ResearchGate

See discussions, stats, and author profiles for this publication at: https://www.researchgate.net/publication/328023681

Modulating Electronic Structures of Inorganic Nanomaterials for Efficient Electrocatalytic Water Splitting

Article *in* Angewandte Chemie · October 2018

DOI: 10.1002/ange.201810104

CITATIONS
54

READS
676

11 authors, including:

Du Xinchuan
University of Electronic Science and Technology of China
26 PUBLICATIONS **2,399** CITATIONS
SEE PROFILE

Jianwen Huang
University of Electronic Science and Technology of China
55 PUBLICATIONS **5,099** CITATIONS
SEE PROFILE

Junjun Zhang
Hefei Normal University
43 PUBLICATIONS **2,860** CITATIONS
SEE PROFILE

Yin Hu
University of Electronic Science and Technology of China
60 PUBLICATIONS **4,242** CITATIONS
SEE PROFILE

All content following this page was uploaded by Du Xinchuan on 23 April 2019.

The user has requested enhancement of the downloaded file.

Check for updates

Water Splitting

International Edition: DOI: 10.1002/anie.201810104
German Edition: DOI: 10.1002/ange.201810104

Modulating Electronic Structures of Inorganic Nanomaterials for Efficient Electrocatalytic Water Splitting

Xinchuan Du[+], Jianwen Huang[+], Junjun Zhang[+], Yichao Yan, Chunyang Wu, Yin Hu, Chaoyi Yan, Tianyu Lei, Wei Chen, Cong Fan,* and Jie Xiong**

Keywords:
d-band theory · defect effects · electrocatalysts · electronic structure · water splitting

Wiley Online Library
© 2019 Wiley-VCH Verlag GmbH & Co. KGaA, Weinheim
These are not the final page numbers!

Electrocatalytic water splitting is one of the most promising sustainable energy conversion technologies, but is limited by the sluggish electrochemical reactions. Inorganic nanomaterials have been widely used as efficient catalysts for promoting the electrochemical kinetics. Several approaches to optimize the activities of these nanocatalysts have been developed. The electronic structures of the catalysts play a pivotal role in governing the activity and thus have been identified as an essential descriptor. However, the underlying working mechanisms related to the refined electronic structures remain elusive. To establish the structure–electronic-behavior–activity relationship, a comprehensive overview of the developed strategies to regulate the electronic structures is presented, emphasizing the surface modification, strain, phase transition, and heterostructure. Current challenges to the fundamental understanding of electron behaviors in the nanocatalysts are fully discussed.

From the Contents

1. Introduction 3
2. Surface Modifications 4
3. Strain Regulation 9
4. Phase Transition 13
5. Heterostructure 15
6. Conclusions and Outlook 16

1. Introduction

Currently, the increasing demand and consumption of traditional energy have led to a variety of serious environmental issues.[1] Sustainable and feasible energy storage and conversion technologies are promising approaches to reduce the dependence on fossil fuels.[2,3] Electrocatalytic water splitting as one energy-conversion technique has been attracting enormous attention.[4,5] Basically, the water splitting process contains two critical electrochemical reactions: the cathodic hydrogen evolution reaction (HER) and the anodic oxygen evolution reaction (OER).[4,6]

From the perspective of electron transfer, HER is a two-electron process while OER is a more complicated four-electron process. Both processes involve the adsorption of reaction intermediates and the dissociation of gases. For example, in basic media, HER starts from the adsorption of water molecules and the subsequent breaking of the H–O bond with one electron (the Volmer reaction). The adsorbed H species continue to react with each other or adsorbed water molecules to form a H–H bond followed by the desorption of a hydrogen molecule via the Heyrovsky reaction or the Tafel reaction.[3,7] As for OER, the multistep reactions, including the dissociation of water molecules, the formation of intermediates, the final desorption of O_2, and the release of electrons/protons, involve the breaking of four H–O bonds and the formation of one O–O bond. Transition-metal atoms usually act as the catalytic sites, and the e_g orbital from the metal d-band can couple with the σ-orbital from the O atom in H_2O in the first step. Then, the intermediates produced in the adsorbed state can undergo a stepwise transformation from *OH to *O, *OOH, and O_2 during the subsequent steps. The reverse process of OER is the oxygen reduction reaction (ORR), which is a reduction process from O_2 to H_2O.[6,8] Undesirably, the electrocatalytic efficiency is typically suppressed by the sluggish kinetics of the electrode reactions, which result in large overpotentials and a great consumption of electrical energy. Although some noble-metal electrocatalysts exhibit high catalytic performance, their high cost and scarcity impede their commercialization.

Over the past decades, the progress to realize cost-effective electrocatalysts has been well developed in two aspects: one is the low loading of noble metals and the other is the development of noble-metal-free catalysts.[8] For the low loading of noble metals, the design of nanostructures, such as core–shell heterostructures and single-atom modulation has become a notable research area,[9–12] not only can it lower the dosage of noble metals but it can also improve the conversion efficiency.[13–16] For the non-noble-metal materials, various strategies mainly including surface modification, strain engineering, phase transition, and heterostructure construction have been explored to enhance the catalytic performance.[17,18] These strategies focus on regulating energy band structure and electron distribution to optimize the electrocatalytic performance.[19,20]

Several groups have recently attempted to define the fundamental relationship between electronic structure regu-

[*] X. Du,[+] J. Huang,[+] Y. Yan, C. Wu, Y. Hu, C. Yan, T. Lei, W. Chen, Prof. J. Xiong
State Key Laboratory of Electronic Thin Films and Integrated Devices
University of Electronic Science and Technology of China
Chengdu 610054 (China)
E-mail: huacrystalring@gmail.com
jiexiong@uestc.edu.cn

C. Fan
School of Materials and Energy
University of Electronic Science and Technology of China
Chengdu 610054 (China)
E-mail: fancong@uestc.edu.cn

J. Zhang[+]
Department of Materials Science and Engineering
Southern University of Science and Technology
Shenzhen 518055 (China)

[+] These authors contributed equally to this work.

The ORCID identification number(s) for the author(s) of this article can be found under:
https://doi.org/10.1002/anie.201810104.

 © 2019 Wiley-VCH Verlag GmbH & Co. KGaA, Weinheim

lation and electrochemical properties.[21] Since the conductivity and adsorption strength (equivalent to the reaction barrier) of the intermediates as two comprehensible behaviors of electronic structure directly determine the reaction kinetics, the electronic structure has been identified as an important descriptor to explain the corresponding catalytic behavior.[22,23] Shao-Horn and co-workers predicted the best OER activity of perovskite oxides at an e_g occupancy value of 1 from the molecule orbital principles.[24] Xie and co-workers highlighted the modulation of charge and spin ordering of 2D ultrathin solids and clarified the structure–property relationship.[5] This research brought electronic-structure regulation further into the focus of the origin of catalytic activity. The spin ordering, energy band structure, and density of state (DOS) intrinsically characterize the electronic behavior. Combining advanced operando spectroscopic techniques and powerful simulation methods, can clearly identify the electronic structure.[25] These methods provide a platform for understanding the atomic-structure-induced regulation of the electronic structure. The derived principles in turn are instructive in designing efficient catalysts for water splitting, CO_2 reduction, and N_2 fixation.[10,15]

In this Review, we summarize the strategies to regulate the electronic structures of inorganic nanomaterials for water splitting, and further to establish the structure–electronic-behavior–activity relationship. The strategies adopted are classified as follows: 1) artificial defects; 2) strain engineering; 3) phase transition; and 4) heterogeneous structure (Figure 1). The working mechanisms of these strategies to corresponding electronic structures are also fully discussed.

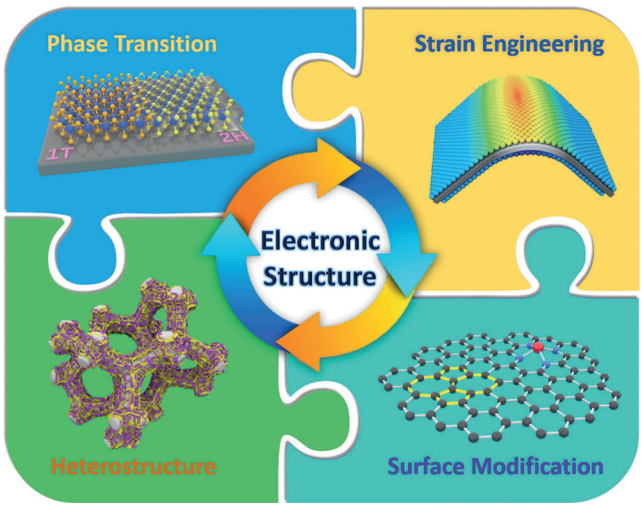

Figure 1. Schematic illustrations of the strategies for regulating electronic structure.

Finally, the challenges of achieving deeper insights into the electronic states of electrocatalysts are highlighted.

2. Surface Modifications

The introduction of artificial defects is regarded as one of the most effective strategies for surface modification. It aims to create more active sites and tune the surface charge-transfer properties.[26] The artificial defects can significantly promote electrocatalytic activity by optimizing the surface-

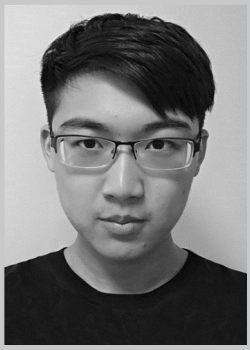

Xinchuan Du is a senior student and will be a Ph.D. student under the supervision of Prof. Yanrong Li at University of Electronic Science and Technology of China. His research focuses on the design and synthesis of functional materials for energy storage and catalysis.

Prof. Cong Fan received his bachelor degree of chemistry in 2008 and Ph.D. degree of organic chemistry in 2013 from Wuhan University, under the supervision of Prof. Chuluo Yang. After a period of post-doctoral research with Prof. Yun Chi and Prof. Qichun Zhang, he joined University of Electronic Science and Technology of China as an Associate Professor in August 2015. His research interests are currently focusing on the synthesis of organic functional materials for Li/Na/K-ion batteries.

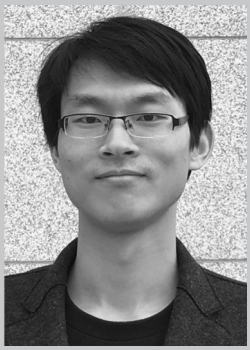

Jianwen Huang received his B.S. degree at University of Electronic Science and Technology of China in 2014. He is currently a Ph.D. student supervised by Prof. Yanrong Li. His research interests are the design of material and structure for energy conversion and storage..

Jie Xiong is a full Professor at the University of Electronic Science and Technology of China (UESTC). He received his Ph.D. degree in materials physics and chemistry from UESTC in 2007, and went to Los Alamos National Laboratory for his postdoctoral research from 2009 to 2011. His research interests focus on the synthesis-structure-property-mechanism of functional nanomaterials and energy materials and their applications. He was elected as the New Century Excellent Talent of Ministry of Education (2013), Sichuan Distinguished Young Scholars (2014), and Distinguished Professor of Sichuan "1000 talent plan" (2014).

© 2019 Wiley-VCH Verlag GmbH & Co. KGaA, Weinheim

These are not the final page numbers!

adsorption ability for reaction intermediates.[27,28] Additionally, the defects can simultaneously tailor the hydrophilic properties of the surface for a better electrolyte contact.[29–31] Considering the diversity of defects, we first discussed the origins of the activity of these artificial defects, which can be generated as artificial vacancies and by heteroatom dopants.

2.1. Surface Vacancies

2.1.1. Non-Metal Materials

Carbon-based electrocatalysts (such as graphene, carbon nanotubes, and porous carbon) are the main non-metal materials used in electrocatalytic reactions. However, the low activity of pristine carbon materials does not meet most application requirements.[32] To tune the original activity of electrocatalysts, vacancy engineering is an effective strategy. In typical 1D and 2D carbon structures, there are two main vacancies types: 1) single-atom vacancies and 2) multi-atom vacancies. The vacancies usually lead to fluctuations in the local electron spin and density, as well as the atomic relaxation at the boundary.[33]

Recently, Xia and co-workers reported a comprehensive analysis regarding the lattice defects in graphene, which involved various single-atom vacancy configurations. According to the charge and spin density analyses, it was found that the regulation of electronic structure by vacancy construction could significantly enhance the catalytic activity of perfect graphene.[34] Baek et al. simulated the edge-molecule orbital configuration of sulfurized graphene nanoplatelets. They proposed that the introduced sulfur atoms are beneficial to the electron-transfer process during ORR.[35] This benefit was attributed to both the significantly polarized highest occupied molecular orbital and the lowest unoccupied molecular orbital levels at the edge sites. These polarized boundaries could provide an ideal electron-transfer capability for ORR electrocatalysis and serve as the active sites. Hu et al. employed carbon nanocages to investigate the roles of intrinsic defects on ORR activity in more detail. This unique microporous cage-structure contains various multi-atom vacancies, including the hole-shaped defects and broken fringes. Notably, this defective carbon nanocages delivered an outstanding ORR activity with a high onset potential (0.11 V vs. the normal hydrogen electrode (NHE)) and an electron transfer number of approximately 2.90 ± 0.10 in 0.1 M KOH.[36] Analogously, the edges of other 2D structural electrocatalysts were also demonstrated as the highly active sites to enhance the electrocatalytic activity.[27]

2.1.2. Transition-Metal Oxides

Transition-metal oxides (TMOs), such as IrO_2, RuO_2, exhibit excellent electrocatalytic performance for OER.[37,38] As a result of the diverse spatial atomic configurations of TMOs (such as spinel-/perovskite-/blende-type structures), the electronic states of the vacancies are complicated. Instead of a simple classification of the complicated structures, herein, the effects of the TMO vacancies for electrocatalysts are highlighted from the perspective of electronic structure regulations.[18]

The formation of ion vacancies can change the original stoichiometric ratio and induce the distortion of local electric field, which would cause electron density redistribution (such as, the valence state and the average number of e_g electrons) at the vacancy sites.[39,40] The occupancy of e_g electron is regarded as a critical descriptor for the HER and OER efficiency. Earlier in the 1980s, Otagawa and Bockris suggested that the application of transition-metal-antibonding-states theory of e_g orbital could be an effective descriptor for the activity of perovskite-type electrocatalysts, especially in OER.[41] The overlap between the σ orbital of oxygen atom in H_2O and the e_g orbital of transition metal is always more stable than that between the π orbital and t_{2g} orbital.[42] Recently, according to a series of simulated data, Shao-Horn and co-workers presented a universal principle to explain the electrochemical OER mechanism, namely the Shao-Horn (SH) principle.[43] It is noticeable that when the number of transition-metal e_g electron is 1, the corresponding metal site will show the best OER and ORR activity in the alkali environment. Consequently, the SH principle leads a bright future for the syntheses of efficient electrocatalysts.

To date, many experimental and theoretical results proved that the filling state of e_g electron of the surface transition-metal sites could play a significant role in tailoring the electrocatalytic activity, especially for the perovskite-type oxides.[44–46] Shao group presented a practical application of the SH principle to select the excellent perovskite-type candidates for OER (Figure 2a).[47] By introducing the vacancies of A sites in $LaFeO_3$, the oxidation state of Fe atoms at B sites was partially increased from Fe^{3+} to Fe^{4+}, as indicated by the Mössbauer spectra in Figure 2b. These induced Fe^{4+} with optimized e_g orbital filling state ($t_{2g}^3e_g^1$) met the expectation of SH principle, so the cation deficient $La_{1-x}FeO_{3-\delta}$ exhibited an optimized catalytic performance with the Tafel slope decreasing from 77 to 48 mV dev^{-1} and the specific activity increasing from 0.061 to 0.364 mA cm^{-2}. Meanwhile, the surface-oxygen vacancies of $LaFeO_3$ had also been found contributing to the electronic-structure rearrangement. Conclusively, the tailoring of the e_g-electron configuration and the adsorption-coupling strength was demonstrated effective for optimizing the electrocatalytic capabilities for both OER and ORR.[44–46,48,49] Furthermore, Yang et al. proposed a geometrical effect to explain the role of oxygen vacancies in $Ca_2Mn_2O_5$ during OER. For the first step, the oxygen atom in an OH^- ion tended to adsorb at the oxygen-vacancy site and then to form an O-octahedron structure around Mn^{3+}.[49] They explained that the Mn^{3+} cations with the $t_{2g}^3e_g^1$ configuration in $Ca_2Mn_2O_5$ could provide a high spin state to overlap the O-p_σ orbital of OH^- ions. Therefore, the oxygen vacancies neighboring the Mn^{3+} cations could act as the adsorption sites during OER process. Notably, it is important that the deeply overlapped orbits could accelerate the ion-exchange and the rate-determining step during OER.[50] To modify the e_g-electronic structure, Xie and co-workers introduced oxygen vacancies into $Ca_{0.9}Yb_{0.1}MnO_{3-\delta}$ by means of Yb doping and hydrogen reduction.[48] They found that the e_g-electron filling degree of

© 2019 Wiley-VCH Verlag GmbH & Co. KGaA, Weinheim

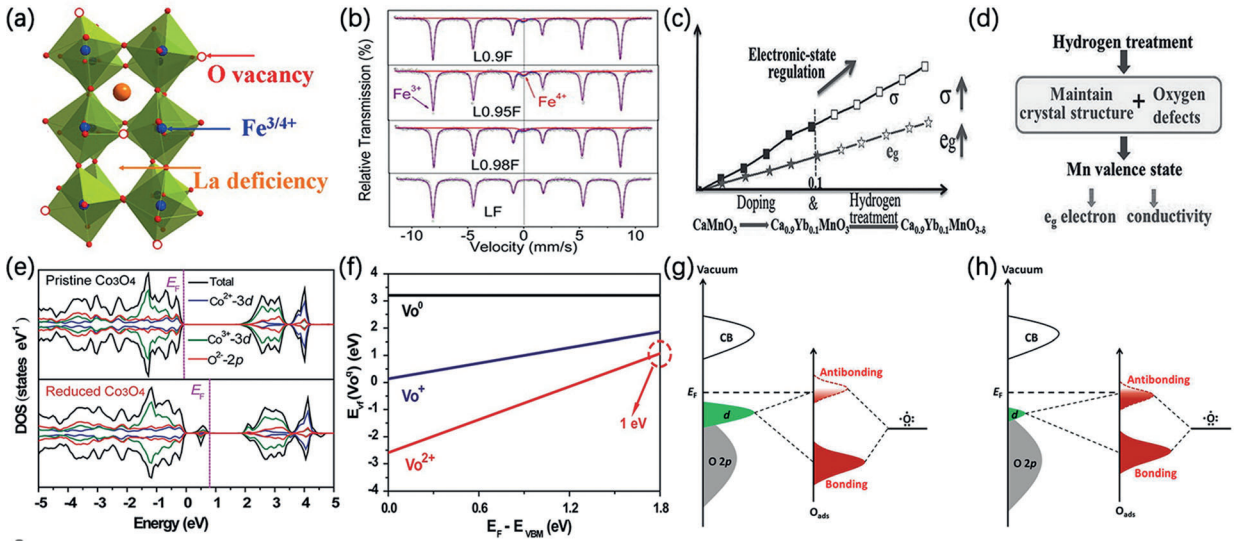

Figure 2. a) The illustration of the O and Fe^{4+} vacancies in perovskites-type $La_{1-x}FeO_{3-\delta}$; b) The Mössbauer spectra of $La_{1-x}FeO_{3-\delta}$ samples at room temperature;[47] Copyright 2016, American Chemical Society. c) The synergistic effect of the hydrogen reduction treatment and Yb-doping on the conductivity (σ) and the number of e_g electrons and d) diagram of the relationship between the hydrogen treatment and the electronic-state regulation;[48] Copyright 2015, Wiley-VCH. e) The PDOS and TDOS results for the reduced Co_3O_4 and the pristine Co_3O_4; f) The simulated formation energy of the O-vacancy with different numbers of electrons present.[31] Copyright 2014, Wiley-VCH. Illustration of the coupling between the d-band and σ-orbital g) before and h) after generating artificial vacancies.[39] Copyright 2016, American Chemical Society.

Mn atoms and the conductivity both showed positive linear relationships with the oxygen vacancy density (Figure 2c). Therefore, the exposed metal sites with an optimized energy-band state showed much lower thermodynamic barriers to form a metal-oxygen bond, so the reaction intermediates could be adsorbed more facilely during OER and ORR (Figure 2d).

Similarly, the electrocatalytic activities of spinel-type and blende-type TMOs can be optimized by tailoring the energy-band configuration and the electron-density distribution.[31,39,51] There are two different effects of artificial vacancies on the reconstruction of energy band. The first one is that the artificial vacancies can generate new electronic states in the original band gap, which are called defect levels. The newly induced states were mainly contributed by the d-band electrons of metal atoms.[51] Therefore, the coupling between the d-band and 2p orbital was strengthened and could result in the reduced thermodynamic barriers for the adsorption of intermediates. It is noteworthy that the split energy level and the increased electronic DOS enhance the intrinsic conductivity of the oxides.[31,40] For instance, Zheng et al. implemented the in situ formation of the oxygen vacancies on Co_3O_4 surface by using $NaBH_4$ as a reductant.[31] Comparing the partial DOS (PDOS) structures, it was found that a new state, close to Fermi level, was induced into the original band gap, which provided a coupling orbital for the 2p electrons of the adsorbed oxygen atom (Figure 2e). Since the formation energy for the bivalent (Vo^{2+}) vacancy was relatively low, the new state was lack of electrons and the filling degree of antibonding orbital under the adsorption state was also reduced (Figure 2f). Consequently, the stronger oxygen adsorption contributed to the faster reaction kinetics with reduced Tafel slope of 72 mV dec^{-1}.[39]

Another one is the orbital interaction. When vacancies are introduced, the energy band structure is tailored by decreasing the d-band electronic density of states and simultaneously increasing the 2p electronic density of states. Because the bonding and antibonding orbits under the O-adsorbed states were both downshifted, the antibonding states under O adsorption could be enhanced accompanying with the weakened free energy barriers for O adsorption (Figure 2g,h).[39] The similar phenomenon also occurred in the n-type semiconductor materials, proved by Chen's study about the OER on the O-vacancy-rich MnO_2.[52] Likewise, the improved activity was found as results of the decline of the d-band electronic density and the reduced adsorption strength of *OH radical.[53,54]

2.1.3. *Transition-Metal Dichalcogenides*

Transition-metal dichalcogenides (TMDs) are promising noble-metal-free electrocatalysts for water splitting.[55] TMDs not only have higher specific surface areas due to the hierarchical structure, but also possess greater plasticity for further activity improvement.[56] Considering the original activity from geometrical edges, activating the inert basal planes of TMDs via defect engineering is a viable strategy to boost the electrochemical performance.[57]

According to the aforementioned SH principle, the activity of the reaction sites can be effectively tailored by vacancy-induced e_g-electron configuration regulation of the active atoms. Xie et al. studied the cation-vacancy effect of $CoSe_2$ nanosheets for OER.[58] After Co-vacancy introduction, the octahedron-coordination field induced the splitting of electron orbits of Co cation into the e_g- and t_{2g}-degenerate states, accompanying with a single-electron-occupied state of

© 2019 Wiley-VCH Verlag GmbH & Co. KGaA, Weinheim

These are not the final page numbers!

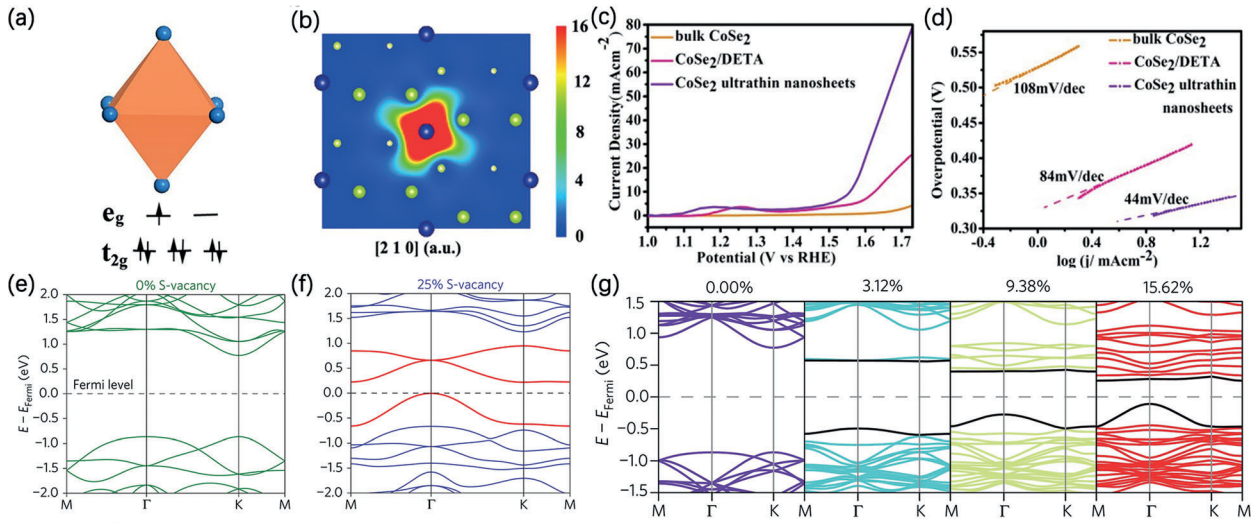

Figure 3. a) The electron-configuration scheme of the Co cation; b) The PAS result at the Co vacancy; c) Linear sweep voltammetry (LSV) curves and d) the corresponding Tafel plots in 0.1 M KOH;[58] Copyright 2014, American Chemical Society. The simulated band-structure scheme of MoS_2 with e) 0% and f) 25% concentration of S vacancies. g) The change in the energy-band structure caused by an increasing of S-vacancy concentration.[60] Copyright 2015, Springer Nature.

e_g orbital, as the SH principle predicted (Figure 3a). In order to provide visual images of the electronic structure at the vacancy area, Xie et al. also used the positron annihilation spectrum (PAS) technique to image the defect region. From the PAS results, the electronic structure around the Co vacancy was clearly pictured and the shorter distinct lifetime of positron suggested that Co vacancy was the main defect type in $CoSe_2$ nanosheets (Figure 3b). Moreover, first-principles calculations revealed that these Co vacancies could serve as active sites for OER. It was further supported by the following electrochemical investigations with the Tafel slope dropping from 108 to 44 mV dec^{-1} and the overpotential (η_{10}) decreasing from 590 to 320 mV (Figure 3c,d). Besides providing the reacting sites, the enriched vacancies could also accelerate the electron transfer, which was further confirmed by the increased DOS near Fermi level and the corresponding electrochemical impedance spectroscopy (EIS) analyses. The same conclusions were achieved experimentally and theoretically as well by our group on the investigations of ion-vacancy effects of ReS_2 nanosheets.[54]

Similar to the TMOs, band gap splitting with the formation of a new defect energy level near Fermi level via vacancy introduction also occurs in TMDs.[59] As reported by Zheng et al., the new energy level could reduce the excited energy of electron from the valence band to conduction band of MoS_2 layers.[60] Moreover, the increase of S-vacancy density could broaden the new energy level, which facilitated more electrons transit to the conduction band, achieving a better conductivity (Figure 3e,f). In another aspect, the related Kohn–Sham orbital of the defect level was located at the S vacancy site with the stronger electron-donating ability, which indicated that the S vacancy of MoS_2 was the adsorption site in Volmer process for HER. Their DFT results further indicated that when 12.5% S-vacancies was introduced, the hydrogen adsorption free energy decreased from around 2 eV to approximately 0 eV. It was conclusive that the enhanced conductivity and more thermoneutral adsorption energy synergistically accelerated the rate of Volmer reaction, ultimately improving the HER efficiency (Figure 3g).

2.2. Heteroatom Doping

In parallel with the strategy of introducing surface vacancies, heteroatom doping is another inspiring motivation for activity enhancement.[61–64] The introduction of heteroatoms or radicals can destroy the periodicity of the lattice, thus it generates a locally changed electronic structure.[65,66] This change can effectively modify the adsorption abilities for the reaction intermediates and thus enhance the electrocatalytic efficiency.[62,63,67] In this section, the relationships among the different doping types, the electronic structure and the electrocatalytic performance are well discussed.

2.2.1. Metal-Atom Dopants

According to the different supporting materials, the metal-atom doping can be divided into two groups: the metal-based materials and non-metal-based materials. Owing to the differences of atomic radii and the electronic configuration of the substituted atoms, the original lattice tends to distort and induce the local electron redistribution. These changes can activate the dopants or neighboring atoms to be the active sites.[66,68] Meanwhile, the electron redistribution is beneficial to charge transfer on the active sites from the electrode interface to the adsorbed reactants.[30,69–71]

In the case of the metal compound based material, doping by the non-noble atoms is one of the most common strategies. Xie et al. reported the V-doped MoS_2 with a modified energy band structure (Figure 4a).[69] As shown in the DOS patterns, the V-atom dopant created a new defect level in the band gap of MoS_2 accompanying with a narrowed energy gap when the

© 2019 Wiley-VCH Verlag GmbH & Co. KGaA, Weinheim

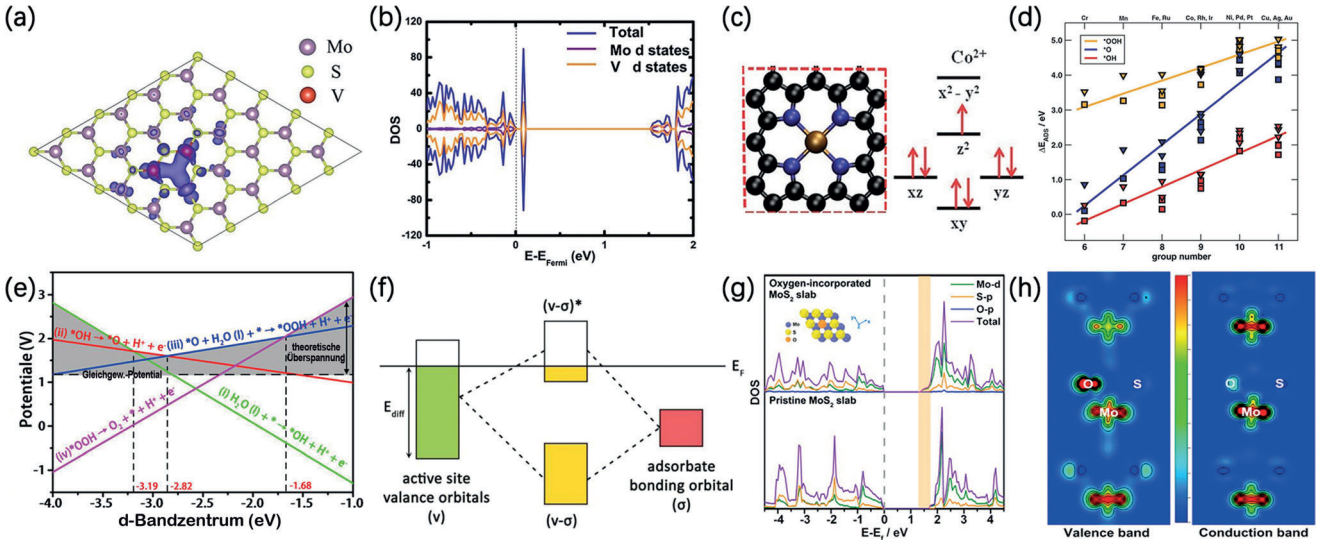

Figure 4. a) The empty-state isosurface (blue shadowing) above the Fermi level of the $V_{0.08}Mo_{0.92}S_2$; b) PDOS diagram of the $V_{0.08}Mo_{0.92}S_2$ nanosheet;[69] Copyright 2014, Royal Society of Chemistry. c) The square coordination environment and the electron configuration of the Co^{2+} ion; d) The trend of adsorption energies with the group of the coordinated transition-metal atoms in graphitic materials with 4 N atoms;[66] Copyright 2011, Royal Society of Chemistry. e) The potential of each reaction step as a function of the d-band center;[72] Copyright 2017, American Chemical Society. f) The orbital hybridization of the valence band of the active sites and the bonding orbital of the adsorbates;[81] Copyright 2014, American Chemical Society. g) The DOS of the oxygen-incorporated MoS_2 slab (top) and the pristine 2H-MoS_2 slab (bottom). h) The charge-density distributions of the valence band (left) and conduction band (right) near the oxygen atom.[64] Copyright 2013, American Chemical Society.

dopant concentration was increased to 8% (Figure 4b). Since the defect level was very close to the bottom of conduction band, the electrons could transfer more easily into the conduction band by virtue of the defect levels. The corresponding isosurface of the empty-state distribution revealed that the interaction between V dopant and neighboring Mo atoms could increase the in-plane conductivity for better charge transport. In addition to the hierarchically structured TMDs, Ding and co-workers also effectively reduced the internal impedance of spinel-type Co_3O_4 and remarkably improved its OER performance by Zn doping.[70] Some similar results were also observed in the perovskite-type electrocatalysts.[30,71] Noble-metal atom is also used as a dopant to tune catalytic activity. Bao et al. reported the Pt-doped MoS_2 with the significant η_{10} value decreasing from 390 to 140 mV.[68] The related calculated results demonstrated that a series of defect levels were induced near Fermi level of the in-plane S atoms, which was quite analogical with the DOS of the active edge S atoms in pure MoS_2. As a result, these reconstructed electronic configurations of the Pt-doped MoS_2 reduced the hydrogen adsorption energy from around 1.83 to approximately 0 eV and consequently boosted the specific activity of HER.

As for the doping on the non-metal materials, the dopant heteroatoms need to embed into the vacancy sites and coordinate with the neighboring non-metal atoms to form a stable configuration as typical single-atom electrocatalysts.[11,12,19,72] At the doping site, the electron polarization could tailor the electronic affinity of both the doped metal atoms and the pristine non-metal atoms, and thereby enhance the reaction charge-transfer kinetics in the vicinity of doping site. Some dangling bonds (incomplete filling electronic orbits) on the anchored metal atoms are usually exposed to the electrolyte solution and tend to couple with the reaction intermediates at the adsorption sites.[66,73] Meanwhile, the commonly used non-metallic-supporting materials derived from carbon-based materials typically exhibit large surface areas and admirable conductivities.[74–76] Therefore, metal-atom-doping can not only increase the active sites through the unsaturated coordination of metal atoms, but also activate the neighboring non-metallic atoms via electronic polarization.[77] For example, Rossmeisl et al. described the dynamic evolution process of electron configuration of Co atom in CoN_4C structure during the four-step ORR (Figure 4c).[66] In the square-planar-coordination field adjacent to the anchored Co atom, the d-orbital of Co^{2+} ion could split into several degenerate sub-orbits. And in the d_{z^2} sub-orbital, the single unaligned electron could act as an adsorption site for the unpaired electrons of O atom and OH^- ion (Figure 4d). As a result, the CoN_4C configuration could thermodynamically accelerate the ORR activity. More interestingly, Wang group developed a method from the perspectives of DOS distribution and the local modification of the d-band center to explore the performance differences of single-atom electrocatalysts with various metallic atom dopants on the non-metallic supporting materials.[72] Based on the antecedent theoretical calculations of the overpotential for the multistep reactions of OER and ORR, they demonstrated that the overpotential could evolve as a function of the d-band center energy (Figure 4e). Moreover, from the curve, it was found that the structure with an energy of around 2.82 eV at the d-band center (relative to Fermi level) could achieve the minimal theoretical overpotential for OER. To prove the above hypothesis, Wang et al. initially constructed a series of structures and found that Ni atoms on the boron monolayer exhibited the closest d-band center to 2.82 eV.[72] Additionally,

© 2019 Wiley-VCH Verlag GmbH & Co. KGaA, Weinheim

These are not the final page numbers!

several other groups concretely confirmed the high performance of Ni-single-atom catalysts even better than other metal-doped configurations on carbon-based substrates.[78–80]

2.2.2. Non-Metallic-Atom Dopants

Non-metallic atom dopants could either directly introduce active sites or activate the nearby atoms to be the active sites.[64,65,81] This activation of nearby atoms is derived from the deformation of the local electronic orbitals and the band structure. For example, Valentin et al. elaborated the transformation of band structure and electron distribution at the doping sites by theoretical analysis.[67] It was found that this tuning could produce certain positive effects on electrocatalytic process. Simultaneously, Qiao and co-workers experimentally investigated the performance of the single-doped graphene electrocatalysts by various non-metal elements. And all the doped graphene demonstrated a better ORR activity than the primary one.[81] Consequently, they generalized a suitable descriptor of E_{diff} for the non-metal electrocatalysts, which was defined as the difference value between Fermi level and the lowest valence-orbital energy at the active sites (Figure 4 f). From the descriptor, the higher valence band leads to the increase in the filling state of antibonding orbital and thus indicates the reinforced adsorption of ORR intermediates. It is desirable to achieve high electrocatalytic performance for the graphene-based ORR electrocatalysts by constructing the active centers with the higher valence-orbital energy level and the smaller value of E_{diff}.

As for the case of doping the non-metal atoms into the transition-metal compounds, a substitution of the native non-metal atoms usually happens, which could result in the charge density redistribution at the doping sites due to different bonding length and electronegativity.[61,64] Xie and co-workers reported that O dopants could drastically improve the HER performance of 2H-MoS_2 nanosheets,[64] where the dopant O atoms unexpectedly redistributed the charge densities in both conduction and valence bands in comparison with those of the original 2H-MoS_2. Further DFT analyses demonstrated that the dopant O could significantly reduce the energy barrier of 2H-MoS_2 nanosheets for hydrogen adsorption from 0.81 to 0.32 eV, along with an increase of charge transfer. These were reflected experimentally by the decrease of the band gap from approximately 1.75 to 1.08 eV and a reduced Tafel slope value from 81 to 55 mV dec^{-1} (Figure 4 g,h). Additionally, Li et al. studied how could the coordination number contribute to the H adsorption energy (ΔG_{H^*}) on the surface sites of N-doped Ni_3S_2.[65] It was found that the stronger coordination capability of N than S along with the larger difference of charge between the bulk and the surface Ni atoms (ΔQ_{Ni}) led to the lower ΔG_{H^*} value. In their experiments, the higher electronegativity of N (3.04) over S (2.58) could generate a larger ΔQ_{Ni} value (0.417 for N site and 0.008 for S site on (100) facet, respectively) of the N-doped surfaces and a stronger hydrogen-adsorption ability (ΔG_{H^*} decreased from 1.086 to 0.036 eV). Besides, the lower coordination number of surface S in Ni_3S_2 nanosheets especially on the (−111) facet with more dangling bonds was also found to contribute to the reduced ΔG_{H^*} (coordination number decreased from 4 to 3, corresponding ΔG_{H^*} reduced from 0.434 to 0.133 eV).

3. Strain Regulation

The lattice strain, either compressive or tensile, can tailor the surface electronic structure via changing the dispersion of surface atoms and their bond lengths.[60,82–84] According to the different strategies of introducing lattice strain, we classify the strains as the inherent strain and the acquired strain. The inherent strain is spontaneously generated during the material preparation process. It was influenced by for example, the hetero-atom substitution, lattice vacancy, phase transformation, lattice mismatch and geometry effect.[85,86] The acquired strain is introduced by the external operation. The induced changes of energy band structure and atomic structure can lead to the optimization of electrocatalytic performance. Notably, tailoring the acquired strain is more flexible than the inherent strain.[86,87]

3.1. The Inherent Strain

How to induce active sites by the inherent strain depends on the properties of materials.[88–90] For the traditional noble-metal materials, the fabrication of nanostructure is an effective strategy to induce lattice stain via increasing the number of the corner- or the edge-site atoms with larger lattice distortion.[91] As for the non-noble metal materials, there are various strategies to introduce the inherent strain, such as, local phase transition, lattice mismatch, vacancy introduction, hetero-atom doping.[82,92–95]

The commercial noble-metal electrocatalysts (such as the Pt/C) usually exhibit a relatively high cost which counteract their existing advantages in performance. To change that, it is feasible to boost their electrocatalytic activities by engineering their nanostructures.[84,89,96–100] Recently, Duan and co-workers increased the record of ORR efficiency by tailoring the rhombohedral geometric structure of the jagged ultrafine Pt nanowires,[89] in which the mass activity and specific activity of the reported electrocatalyst reached 13.6 A mg_{Pt}^{-1} (at 0.9 V vs. NHE) and 11.5 mA cm^{-2}, respectively. And it was found that the stress residual on the zig-zag Pt nanowires was caused by the post-annealing and the electrochemical dealloying processes, which compressed the lattice spacing of Pt (111) plane from 0.23 to 0.21 nm. Furthermore, the first principle calculations showed that the d-band center of the Pt nanowires downshifted along with the decrease of surface adsorption energy.[84,100–103] Back in the 1990s, the relationship between the chemical activity of the transition-metal surface and the filling state of d-band was proposed by Nørskov and Hammer.[97] Later, they further elaborated the relationship between the transition d-band center and the adsorption free energy.[98] The d-band center theory predicted that the tensile lattice strain could reduce the d-band width of the late transition metal. As a result of the charge conservation during the distortion, the d-band could shift to preserve its filling degree relative to Fermi level. Thus, the orbital filling

 © 2019 Wiley-VCH Verlag GmbH & Co. KGaA, Weinheim

These are not the final page numbers!

condition of bonding and anti-bonding orbits exhibited the significant influence on the adsorption bond strength and thus on the electrocatalytic activity.[84,99,100]

Although the d-band center theory could explain most inherent strains, the recent experiments and theoretical simulations showed that the traditional d-band center model was not suitable for some certain cases. For example, two typical representatives beyond the traditional d-band center models are the PtNi twinned nanostructure and the Pt/PtPb core–shell structure.[91,104–106] The twinned PtNi nanocrystals exhibited an interesting geometric structure and an entirely different electrocatalytic property.[104] Taking octahedra and icosahedra Pt_3Ni nanocrystals as the examples, the electrocatalytic efficiency of the icosahedral one was 50% higher than that of the octahedral one. Besides the inherent strains induced by the different ratio and coordination numbers of the edge and corner atoms mentioned above, another important factor is the surface strain.[91] The simulated results demonstrated that the octahedral and icosahedral geometries showed a reverse state of surface strain (surface compressive strain on octahedral nanoparticles, while surface tensile strain on icosahedral nanoparticles). DFT calculations further confirmed that the *OH adsorption energy barrier and d-band center of the icosahedra Pt twinned crystal were optimized by the in-plane stress.[105,106] In addition to the twinned crystal, Adzic and co-workers fabricated a core–shell structure with a Pt shell covering internal PtPb compounds core (Pt/PtPb). Due to the geometric and ligand effects, the tensile stress was remained in the Pt shell.[107] The enlarged bond length and the shifted energy-band not only accelerated the oxygen reaction rate but also created additional adsorption sites. More studies also demonstrated that the expanding strain on the stepped surface of metal electrocatalysts could reduce the adsorption barriers of reaction intermediates.[108,109]

The local phase transformation can produce the inherent strain, which induces band distortion in the non-noble-metal polymorph electrocatalysts to affect the electrocatalytic performance.[110] For example, the synergistic effect of the inherent strain and the phase transition could tailor the thermodynamic adsorption processes of intermediates.[83] Through calculating the DOS evolution process of 1T′-MoS_2 before and after hydrogen adsorption under different inherent strains, Kuo et al. found that the positions of the bonding and anti-bonding states were not apparently shifted under the inherent strain, even when the PDOS was enhanced to Fermi level.[111] It could not be explained by d-band theory. But from the perspective of better conductivity, the calculated reaction barrier dropped from around 0.75 to approximately 0.25 eV. A similar study focusing on the movements of conduction band of monolayer MoS_2 and NbS_2 was also reported by Wang group.[112] They derived the proportional relationship between the change of free energy and the electron affinities (E_{ea}) by thermodynamic analyses. The tensile strain derived downward shift of the conduction-band minimum could directly result in the increase of E_{ea} value, which further strengthened the weak hydrogen adsorption of pristine materials and reduced the reaction barriers of HER.

The heteroatoms and lattice vacancies can generate the inherent strain in the surrounding lattices. The elongated or shortened bond length indirectly tunes the electron configuration and the adsorption ability of the surface atoms for electrocatalysts.[60,90] Qiao and co-workers employed the cation exchange methodology to enrich oxygen vacancies on the CoO (111) surface, which could directly induce tensile strain to the nearby lattices.[90] As a result, this approach facilitated the upshift of the 2p band of oxygen atoms and intensified the Co−O adsorption bonding. Thus, the oxygen atoms have relatively low possibility to adsorb H atoms and the CoO exhibited an optimized hydrogen-adsorption free energy from −1.8 to about 0 eV and a decreased η_{10} of 73 mV. Meanwhile, Nørskov and Zheng groups identified the individual effects of vacancies and tensile strain.[60] It was verified that the vacancies could create new states in the original band gap while the tensile strain could subtly tailor the band structure. Clearly, the cooperative effect between the vacancy and inherent strain from the above two examples is beneficial in improving the electrocatalytic ability. The performance of non-metallic electrocatalysts can also be tailored by the inherent strain regulation.[88,113–116] Du and co-workers reported a method to induce the compressive strain of g-C_3N_4 by iso-electronically doping of Si atoms.[88] From the DFT simulations of the varied lattice strain between ±5%, the band gap and adsorption free energy showed a declined trend when the inherent strain intensity was increased (Figure 5a,b). Meanwhile, they discussed the influence of different hydrogen-coverage states on the adsorption energy besides the inherent strain (Figure 5c), where the positive synergistic effect between the hydrogen-coverage states and inherent strain was confirmed by the results of adsorption energy. Furthermore, a dynamic electrocatalysis experiment by changing the surface strain of g-C_3N_4 was carried out. It was revealed that the cycling of the adsorption and desorption of hydrogen atoms on compressed or stretched g-C_3N_4 could indeed accelerate the electrocatalytic reaction rate (Figure 5d).

As has been established, the core–shell structure can bring in the inherent strain, thus it facilitates the upshift of the d-band center and enhances the electrocatalytic activity.[102,117] For instance, Strasser and co-workers demonstrated the Pt/PtCu core–shell structure as a high-performance ORR electrocatalyst. Owing to the lattice mismatch, the compressive stress was induced by the Pt-enriched layer via the smaller interatomic distance of Pt. According to the d-band center theory, the inherent strain contracted the d-band width. As a result, the weakened adsorption strength between the Pt-enriched layer and the O-containing intermediates boosted the ORR efficiency.[117,118] The similar core–shell structures were also used to enhance the stability of alloy nanoparticles.[102,103] Alternatively, the alloying of Pt with the rare-earth elements or early transition-metals is another effective strategy to boost the ORR performance.[119] The polycrystalline alloys of platinum with these elements showed changed oxygen-adsorption free energies. As the d-band center theory predicted, the volcano-shaped relationship was developed between the d-band center energy and the specific activity.[120–122]

© 2019 Wiley-VCH Verlag GmbH & Co. KGaA, Weinheim

These are not the final page numbers!

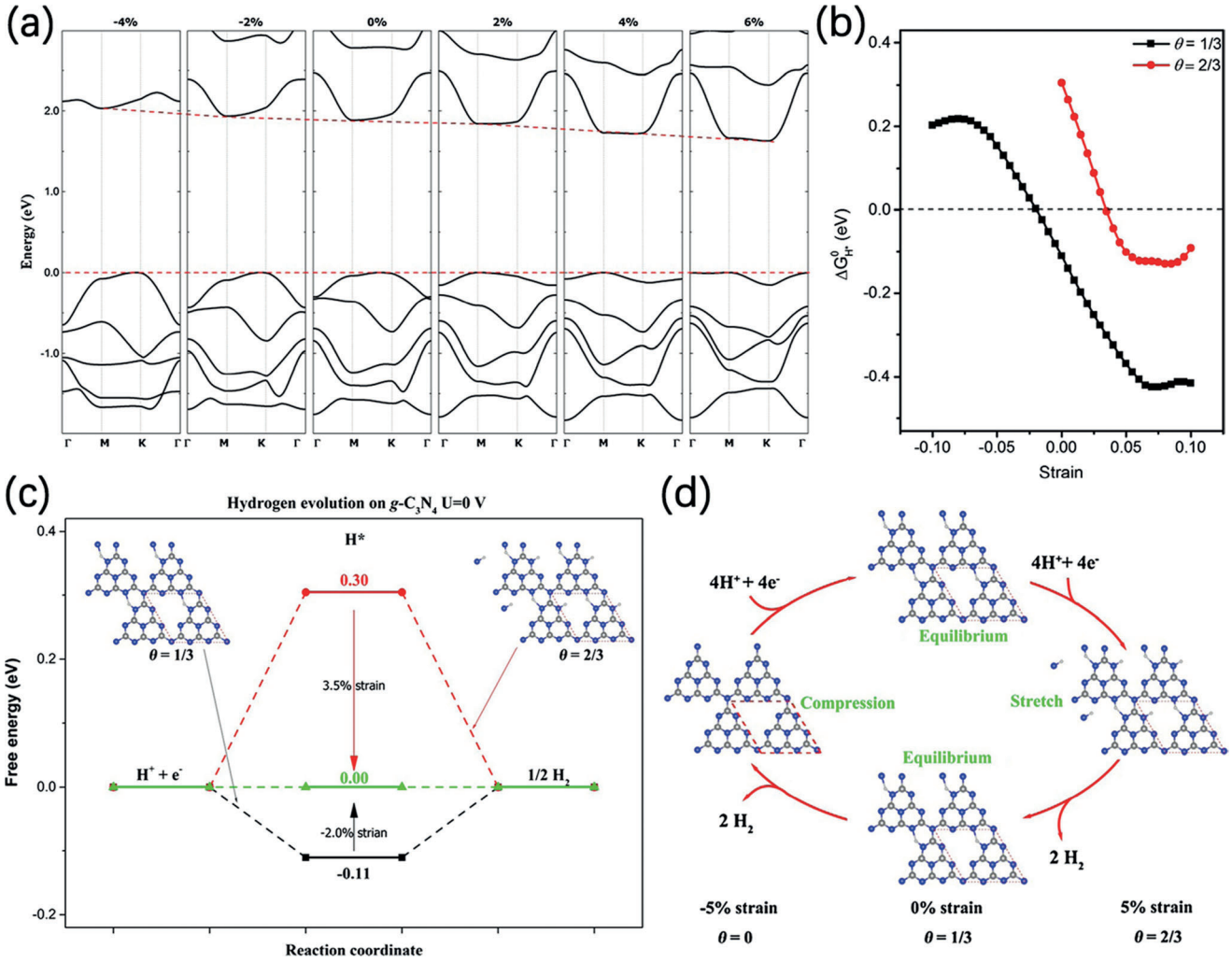

Figure 5. a) The energy-band structures of g-C_3N_4 with 4–6% strain intensity; b) The ΔG_{H^*} values versus the intensity of strain under the H-coverage ratio (θ); c) The simulated HER energy-barrier scheme for g-C_3N_4 under different H-coverage ratios; d) The dynamic-strain-cycle scheme of g-C_3N_4 during HER.[88] Copyright 2015, Elsevier Inc.

Apart from the above-discussed inherent strain effects on the electrocatalytic performance of Pt-based materials, the interface engineering between the substrate and loaded catalysts is another impressive method to control the inherent strain.[123–125] As for TMOs, it noted that some TMOs obey the band center theory. Yang and co-workers found the evolution of the inherent strain was correlated with the OER activity.[123] In the IrO_2-coated MoO_2 nanorods, the inherent strain of IrO_2 from the lattice mismatch between MoO_2 and IrO_2 could be controlled by the size of IrO_2 particles. And the extrusion of the oxygen octahedrons induced by the compressive strain could lead to the decreased binding energy of Ir $4f_{7/2}$ and the down-shift of d-band. Furthermore, the X-ray photoelectron spectroscopy (XPS) and X-ray absorption near edge structure (XANES) results demonstrated that the charge transfer from MnO_2 to IrO_2 could result in a higher oxidation state of Mn element and a lower oxidation state of the Ir element. These active catalyst–substrate interactions directly boost the OER catalytic activity with a 3.7 times increased specific mass activity than that of pure IrO_2.[124] As for the TMDs, the ones with the special 2D structure were often selected as typical examples to investigate the relationship between the inherent strain and electronic structure.[111,126–129] Chen et al. adjusted the inherent strain of MoS_2 via the lattice mismatch between MoS_2 and Au substrate (Figure 6a).[125] Based on the results from the high-angle annular dark field scanning transmission electron microscope (HAADF-STEM) and high-resolution STEM, they calculated the S-Mo-S bonding angle for MoS_2 monolayer and proved the existence of atom migration and in-plane strain (Figure 6b,c). Meanwhile, they found that the charge-density distribution was regulated by the existence of lattice strain, atom migration along with the ohmic contact between MoS_2 and Au substrate (Figure 6d,e). Moreover, by simulating the MoS_2 model with different S-Mo-S bonding angles, they explained that the reverse migration between S and Mo atom could gradually decrease the band gap from 1.8 to 0 eV and reduce the ΔG_{H^*} value from approximately 0.5 to around 0.2 eV (Figure 6f,g). As a result, the optimized ΔG_{H^*} value and the superior conductivity of MoS_2/Au achieved a reductive Tafel slope of 46 mV dec^{-1}. Similar results from other TMDs (such as WS_2 and $MoSe_2$) further verified that

© 2019 Wiley-VCH Verlag GmbH & Co. KGaA, Weinheim

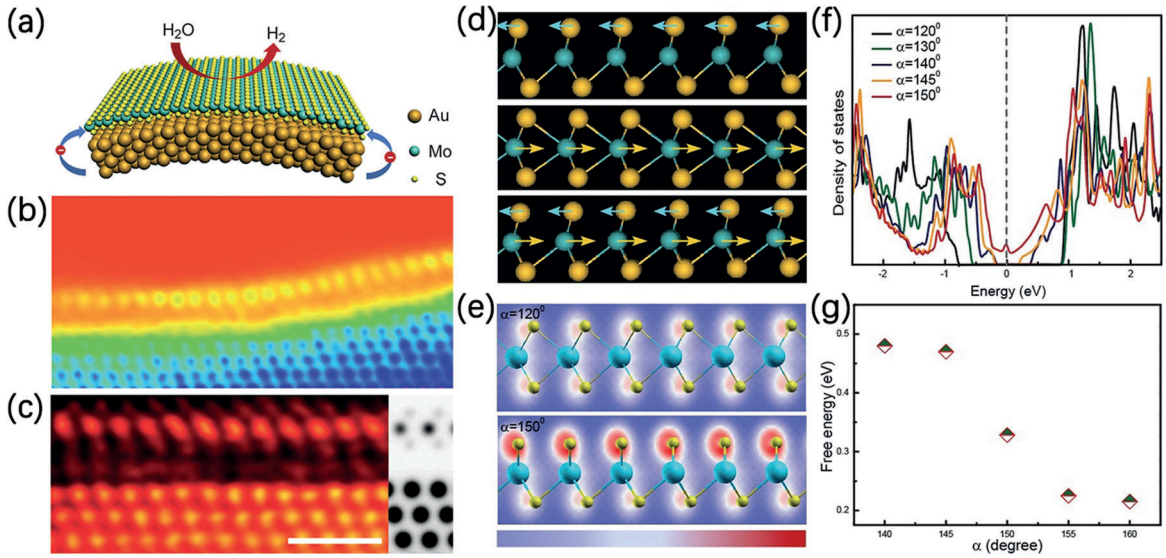

Figure 6. a) The single-layer MoS_2@NPG; b) The cross-sectional HAADF-STEM image and c) HR-STEM image of single-layer MoS_2@NPG. Scale bars: 1 nm; d) The distorted lattice structures with S translation (top); Mo translation (middle panel); S and Mo translation (bottom). e) The charge-density distributions in pristine monolayer MoS_2 and bent monolayer MoS_2. f) The DOS distribution and g) the free energy of hydrogen adsorption under a series of S–Mo–S bond angles α.[125] Copyright 2014, Wiley-VCH.

introducing inherent strain was a fruitful way to enhance the HER performance.[111,129]

3.2. The Acquired Strain

The acquired strain is admirable in electrocatalytic process, owing to the feasible controllability and operability. In recent years, different physical or chemical methods to tailor the acquired strain from external operation have been proposed.[86,87,117,130] The controllable substrate deformation is the main way to introduce the mechanical strain into the electrocatalyst films. Bard and co-workers used the NiTi-shape-memory alloy (SMA) substrate to load the Pt nanofilms as the ORR electrode,[117] where the SMA exhibits the reversible deformation performance as a function of temperature. When the SMA was bended, the tensile or compressive strain could be transmitted from substrate to the deposited Pt membrane. By controlling the deformation degree, they found that the compressive strain could prominently reflect a 27 mV positive shift of the half-wave potential and a 52% enhancement of the kinetic rate constant than pristine Pt, which was consistent with the theoretical predication.[98,104] Furthermore, to visually illustrate the effect of acquired strain, Peterson and co-workers designed a strain-regulable electrolytic cell to in situ measure the electrocatalytic ability under different strain environments,[131] where the poly(methyl methacrylate) (PMMA)-loaded tungsten carbide (WC) with an outstanding stretch ability was used as the HER electrocatalyst.[86] In particular, the strain intensity was controlled within ±1.6% by a universal tensile tester. From the cyclic voltammetry measurements, they found a positive relationship between overpotential and strain with the overpotential shifting 10–20 mV per 1% strain. It was noting that the compressive strain increased the catalytic activity, while the tensile strain contributed the opposite effect. Further DFT simulations verified that the d-band center was downshifted along with an increase in the axial compressive strain.

Besides the substrate-treating strategy for the acquired strain, some physical methods such as external electric field and magnetic field have also been applied to induce the structure strain.[86,87,130,132] Frauenheim and co-workers investigated the relationships among external electric field, magnetic moment and in-plane strain in MoS_2 nanoribbons via spintronic methods,[130] where the PDOS and band structure evolution predicted that the external electric field could tune the internal polarization and the magnetic moment spin. Furthermore, the effect of the introduced electric field on the HER activities for MoS_2 and $MoSe_2$ was experimentally verified by Mai and co-workers.[86,132]

Chemical treatments can also control the acquired strain. Cui and co-workers applied a novel ion-inserting strategy for $LiCoO_2$ to bring in the distortion of atomic structure during the lithiation and delithiation processes.[87] They firstly deposited Pt nanoparticles on the $LiCoO_2$ substrate. Then, the delithiation and stretching of $LiCoO_2$ substrate could induce the tensile strain in the (111) plane of Pt particles. Notably, the compressive stress was obtained by a reversed method (Figure 7a,b). Consequently, from the results of the electrostatic repulsion between lithium ion and Co–O octahedron, the interplanar distance of $LiCoO_2$ (003) plane extended from 0.469 to 0.482 nm, ultimately generating ≈5% lattice strain into the Pt nanoparticles. Meanwhile, the XPS and theoretical simulations proved that when the strain was changed from 5% to −5%, the d-band center of Pt could downshift from −2.32 to −2.69 eV (where the initial value is ca. −0.25 eV) (Figure 7c). Comparably, the approximately 5% tensile strain could lead to an upshift of approximately 0.17 eV of the d-band center. Furthermore, they calculated the results of the adsorption energy barriers for the adsorp-

© 2019 Wiley-VCH Verlag GmbH & Co. KGaA, Weinheim

These are not the final page numbers!

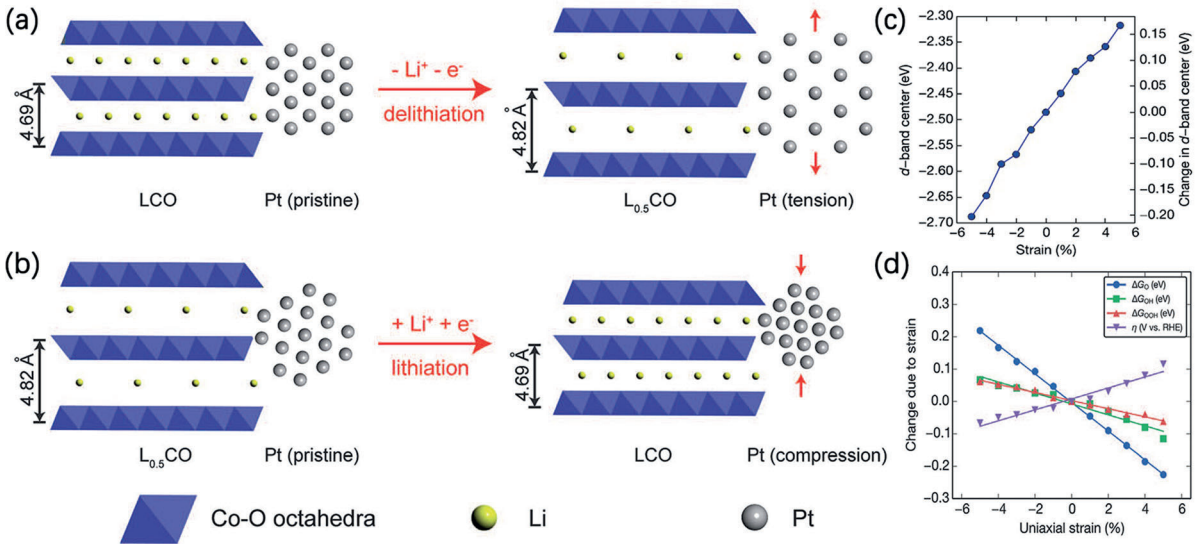

Figure 7. Schematic representation of how a) delithiation and b) lithiation processes induce in-plane strain in Pt nanoparticles and change the layer spacing of $LiCoO_2$ (LCO) substrates. c) Illustration of the relationship between the strain intensity and the energy of the d-band center. d) The relationship between the binding energies of OER intermediates and the overpotential (η) versus the strain intensity.[87] Copyright 2016, American Association for the Advancement of Science.

tion energies of *O, *OH, and *OOH intermediates on the strained surface, and the results showed accordance with the analysis of the d-band model. As a consequence, the adsorption energies with the rational compressive strain could lead to the decreased overpotential for OER (Figure 7d).

4. Phase Transition

The properties of electronic structure are highly dependent on the crystal phases of materials, owing to the different charge distributions from various atomic configurations.[133,134] The adjustment of crystal phase usually tailors the surface adsorption properties and the charge states, which can lead to better conductivity and higher surface activity.[135,136] Therefore, phase engineering is usually identified as a promising method to enhance the electrocatalytic activity.[136,137]

There are several ways to control phase transitions. The exfoliation is one of the most common strategies to induce phase transformation, especially for the layered TMDs. Taking bulk MoS_2 as an example, the 2H-phase is the thermodynamically stable state whereas the basal plane of the 2H-MoS_2 is inert for hydrogen evolution. It was found that the phase transition from the 2H to 1T phase could activate the basal plane and enhance its HER activity.[136,138] As early as the 1970s, a chemical method via lithium intercalation was reported to exfoliate the bulk MoS_2.[139,140] After the insertion of lithium atoms into MoS_2 interlayers, the rearranged electronic structure and the intra-strata shear strain synergistically derived the phase transition.[137,141–143] Besides the exfoliation strategy, Reed et al. reported another mechanical deformation method to realize the phase transition of TMDs.[144] In 2014, Suenaga et al. developed a new strategy for phase transition via electron beam irradiation. The irradiation could introduce external electrons and then transform the phase from 2H-MoS_2 to 1T-MoS_2 with high crystallization.[145] In the same year, Fang and co-workers found that the plasmonic hot-electron injection from the Au nanoparticles could lead to the phase transition of TMDs under light irradiation due to the local plasmon resonance excitation.[146] Notably, the phase transition of TMDs was also observed under heating treatment and epitaxial growth conditions.[147–150]

As mentioned above, the phase transition of TMDs from the 2H to 1T phase was usually caused by the introduction of hot electrons. To investigate the influence of inserted hot electrons to electronic structures, many pioneering works were reported using theoretical methods. Lau group calculated electronic band structures for the 2H-, 1T- and 1T′-MoS_2 (Figure 8a).[155] When the phase transmitted from 2H to 1T, the original band gap disappeared due to the partially overlapped conduction-band minimum and valence-band maximum. On the other hand, the 1T′ phase as a disordered configuration derived from 1T phase showed a narrow band gap of 0.09 eV, which meant a decreased conductivity compared to 1T structure. Meanwhile, as demonstrated by Seifert et al., when a hot electron was injected in the tri-prism MoS_6 unit of 2H-MoS_2, the inherent degenerate state could no longer be the lowest energy state. According to the Jahn–Teller effect, the MoS_6 unit would transform to the octahedron obeying the minimal energy principle (Figure 8b).[151] Thus the crystal phase of MoS_2 spontaneously transformed from the 2H to the 1T state. Notably, the formation energy of the 1T′ phase was 0.15 eV lower than that of the 1T phase per MoS_2 unit. Therefore, the 1T phase could evolve to the 1T′ phase in certain conditions.[143] Conclusively, the formation of a new phase with enhanced conductivity is a viable way to accelerate the reaction kinetics and realize lower reaction barriers for HER (Figure 8c).[136] Besides the hierarchical

© 2019 Wiley-VCH Verlag GmbH & Co. KGaA, Weinheim

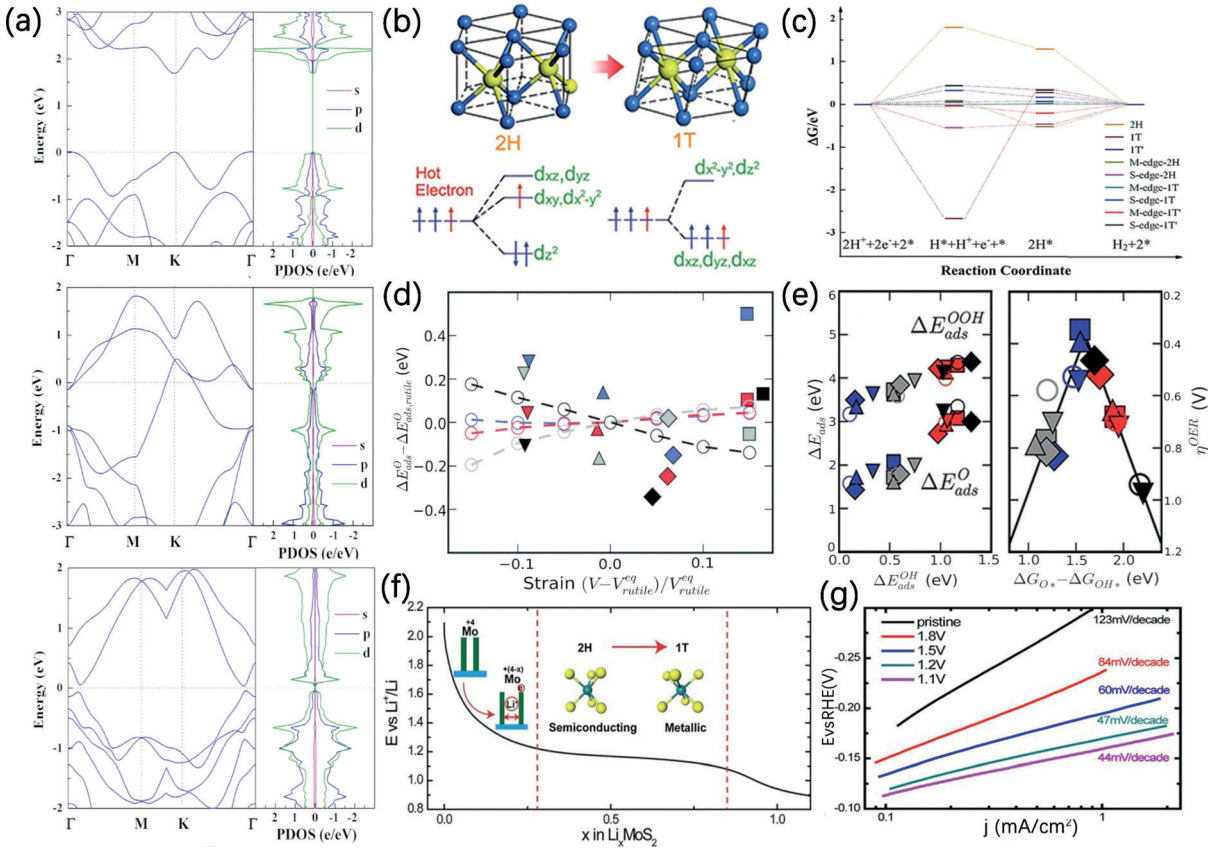

Figure 8. a) The energy-band structure and PDOS of the 2H-MoS_2 (top), 1T-MoS_2 (middle), and 1T′-MoS_2 (bottom);[155] b) Illustration of the transition from the octahedral to the triangular-prism MoS_6 structure and the simultaneous translation of the electron configuration.[151] Copyright 2011, American Chemical Society. c) The simulated free-energy profile of the HER process on the edges and basal planes of 2H-, 1T-, and 1T′-MoS_2;[155] Copyright 2014, Royal Society of Chemistry. d) The relationship between the adsorbed energies (ΔE) of different intermediates and the intensity of strain for various phases; e) the relationship between different ΔE values (left) and the volcano-shaped relationship between over potential and oxygen evolution (right).[152] Copyright 2015, Royal Society of Chemistry. f) The galvanostatic discharge curve and the change in interlayer spacing during the lithiation process; g) The Tafel slope of the pristine 2H-MoS_2 and lithium-inserted MoS_2 under different anode potentials;[137] Copyright 2013, National Academy of Sciences.

materials, IrO_2 also has different phases, such as the rutile type, niobite type, which have different DOS distributions and electrocatalytic activities for OER. For example, the rutile-type IrO_2 has more t_{2g} states near Fermi level. It is noteworthy that the enhanced t_{2g} states could weaken the e_g anti-bonding state and the O-coupling strength.[152] Thus, the OER barriers will be reduced (Figure 8d,e). Summarily, the redistribution of t_{2g}-band electrons can indirectly tune the OER activity.

The mechanism of catalytic reaction and the distribution of active sites could be essentially changed by the phase transition.[136,138] Taking the work of Cui and co-workers as an example, they verified how the phase transition of MoS_2 had different effects on the HER electrocatalysis.[137] Based on the traditional electrochemical lithium intercalation, they controlled the lithiation process by anode potential during the galvanostatic discharge in a pouch battery cell (Figure 8f). The crystal phase was changed from the pristine MoS_2 to the Li_xMoS_2, which was confirmed by the XPS and TEM results. During the phase transition from the 2H-MoS_2 to 1T phase in Li_xMoS_2, the incoming electrons accumulated in the MoS_2 layers and could increase the d-band filling degree for the Mo atom. Meanwhile, the oxidation state of the Mo element was reduced and it thus could decrease the reaction barriers for HER. Consequently, the Tafel slope significantly dropped from 123 to 44 mV dec^{-1} (Figure 8g). And the dramatic decrease in the Tafel slope indicated the different rate-determining steps of HER for the 2H- and 1T-phase MoS_2.[153] Jiang et al. pointed out that the S sites in 2H- and 1T-MoS_2 had different hydrogen adsorption free energies (0.78 eV for 2H-MoS_2 and 0.62 eV for 1T-MoS_2). The simulation results therein for HER showed that the Volmer-Heyrovsky reaction exhibited the higher priority than the Volmer-Tafel reaction on the 1T-MoS_2 surface.[136] In addition to the different reaction mechanisms, Chhowalla et al. verified the difference in the active-site distribution between the 2H- and 1T-MoS_2. Through partially oxidizing the edge of the 1T- and 2H-MoS_2, the electrocatalytic performance of 2H-MoS_2 sharply dropped while the 1T-MoS_2 still showed a stable HER activity, which demonstrated that the active sites of 1T-MoS_2 nanoparticles were located on the basal plane rather than the edge sites in 2H-MoS_2.[138,154] The same results were also proved by the simulated ΔG_{H^*} values.[60,155] The relationship between the lattice structures and the corresponding catalytic activities for

© 2019 Wiley-VCH Verlag GmbH & Co. KGaA, Weinheim

These are not the final page numbers!

the two phases of $CoSe_2$, namely the cubic (c-$CoSe_2$) and octahedral (o-$CoSe_2$) phases, was recently reported by Xie et al.[135] By analyzing the R-space map of the o-$CoSe_2$ and c-$CoSe_2$ phases from the X-ray absorption fine structure (XAFS), they demonstrated that the c-$CoSe_2$ phase had a larger Co–Se bond length (2.13 Å) than that of the o-$CoSe_2$ (2.08 Å). Notably, the larger bond length could boost the local electron density around Se atoms. As a result, the activated Se atoms showed a smaller reaction barriers (−0.163 eV for water adsorption and ca. 0.05 eV for hydrogen adsorption), further supported by a lower Tafel slope of 85 mV dec^{-1} for HER.[156–158] Conclusively, the overall electron-transporting kinetics could be optimized by the phase transition. From the simulated results of band structure, the narrower band gap of the c-$CoSe_2$ phase indicated that the c-$CoSe_2$ phase could have better intrinsic conductivity, which was further proved by the EIS results.

5. Heterostructure

Design of heterostructure is an important strategy to construct the active interface for electrocatalysis, which can create new catalytic sites by tailoring the interface electronic structure and lattice strain, as well as enhance interface charge-transfer kinetics.[18,148,159,160] During the past years, the different structural features (such as, core–shell, yolk–shell, hetero-layer stacking, surface particles) have been fabricated to realize the desired electrocatalytic performance.[147,148,161] For a deeper insight into the heterostructure strategy, more and more experimental and theoretical efforts have been paid to clarify the relationship between the heterostructure and catalytic activity. In this section, the relationship is summarized from the perspective of nanostructure-induced electronic structural changes.

According to most of heterostructure electrocatalysts, the active semiconductive material are usually loaded on conductive materials. This contact between semiconductor and conductive materials is referring to the Mott–Schottky contact which can lead to the interfacial-energy-band distortion and charge migration between two materials.[162–165] However, only a small number of heterostructures can induce the electronic structural changes and thus increase the catalytic efficiency by reducing the contact resistance. After the detailed analysis, it is conclusive that the matched electronic affinities and Fermi level of the materials are the precondition to fabricate the efficient Mott–Schottky electrocatalysts.[162–164] Mai and co-workers designed a MoB/g-C_3N_4 Mott-Schottky electrocatalyst to improve the HER efficiency, where they illustrated the band structure of MoB and g-C_3N_4 before and after Mott-Schottky contact (Figure 9a,b).[164] Because the electronic affinity of MoB under vacuum was larger than that of g-C_3N_4, the electrons could transfer from g-C_3N_4 to MoB and thus the electron-enriched MoB could catalyze HER more efficiently. And the simulated results of charge density showed that the positive (red) and negative (blue) charges could accumulate on both sides of the interface (Figure 9c). Further XPS and energy-loss near-edge structure (ELNES) analyses clearly demonstrated the increased electron density of MoB and the existence of Schottky structure. In summary, it was confirmed that a Mott–Schottky structure could contribute to the electron transportation and accelerate the HER kinetics. Similar to the Mott-Schottky contact, Zhu and co-workers reported a vertical heterojunction of graphene loaded n-type MoS_2 (n-MoS_2). Since the stronger electron affinity of graphene than n-MoS_2, electrons could transfer from n-MoS_2 to graphene spontaneously, resulting in the formation of an internal electric field near the interface.[166] Because of the high potential state of MoS_2 layer, the electrons could transfer facilely from electrode to graphene and then to the MoS_2 during the electrolysis. The excessive negative charge density of MoS_2 layer could dramatically shift the hydrogen adsorption energy to a more thermoneutral value. Meanwhile, the electron offset of similar structures has also been confirmed by other experimental and theoretical results.[167,168] Recently, Yao et al. reported the heterostructure of the defective graphene (DG) and the NiFe-layered double hydroxide nanosheets (NiFe LDH-NS).[159] The electron transportation could separate and redistribute electrons and holes in DG and NiFe LDH-NS. The increased electron density on DG favors the HER performance, while the enriched holes on NiFe LDH-NS could enhance the OER performance. The heterostructure is one of the breakthroughs for preparing efficient bifunctional electrocatalysts.

The strong electron interaction of heterostructures could rearrange the electronic states and consequently optimize the adsorption and conductivity for electrocatalyst materials.[160,169] Owing to the strong electron coupling, the DOS distributions of the active atoms are tailored, and the physicochemical properties are optimized at the contact position. The strong electron interaction usually occurs in the materials that have incompletely-filled d or f sub-shells and narrow energy bands. In these materials, the Coulomb interaction between electrons is not negligible and so the mean field theory is no longer applicable.[170] To better analyze and understand the catalytic process, the local-density approximation and Hartree–Fock theory analysis are often required. A typical example reported by Fu et al. was the heterostructure constructed by the reduced graphene oxide, molybdenum carbide (Mo_2C) and nitride (Mo_2N).[169] And this heterostructure electrocatalyst showed excellent catalytic activity for HER and the outstanding stability over a wide range of pH values. Meanwhile, the minute size of the N–Mo–C heterojunction could provide more active sites for electrocatalytic reactions (Figure 9d). As a result, the holey reduced graphene oxide not only provided abundant surface for the grown of N–Mo–C but also facilitated the charge transportation of the catalysts. The simulated results revealed that the reaction barrier for HER was decreased to a near-zero value at the Mo_2N–Mo_2C interfacial sites (Figure 9e), and a better charge-transfer capability was achieved from the higher DOS near Fermi level (Figure 9f). The same law has also been confirmed by Fu's work.[160] They drew a conclusion that the higher DOS at the Fermi level could drive the electrocatalysts to be more conductive and active.

For better electron transportation, it is a common strategy to use carbon nanotube, carbon cloth, nickel foam, and other

 © 2019 Wiley-VCH Verlag GmbH & Co. KGaA, Weinheim

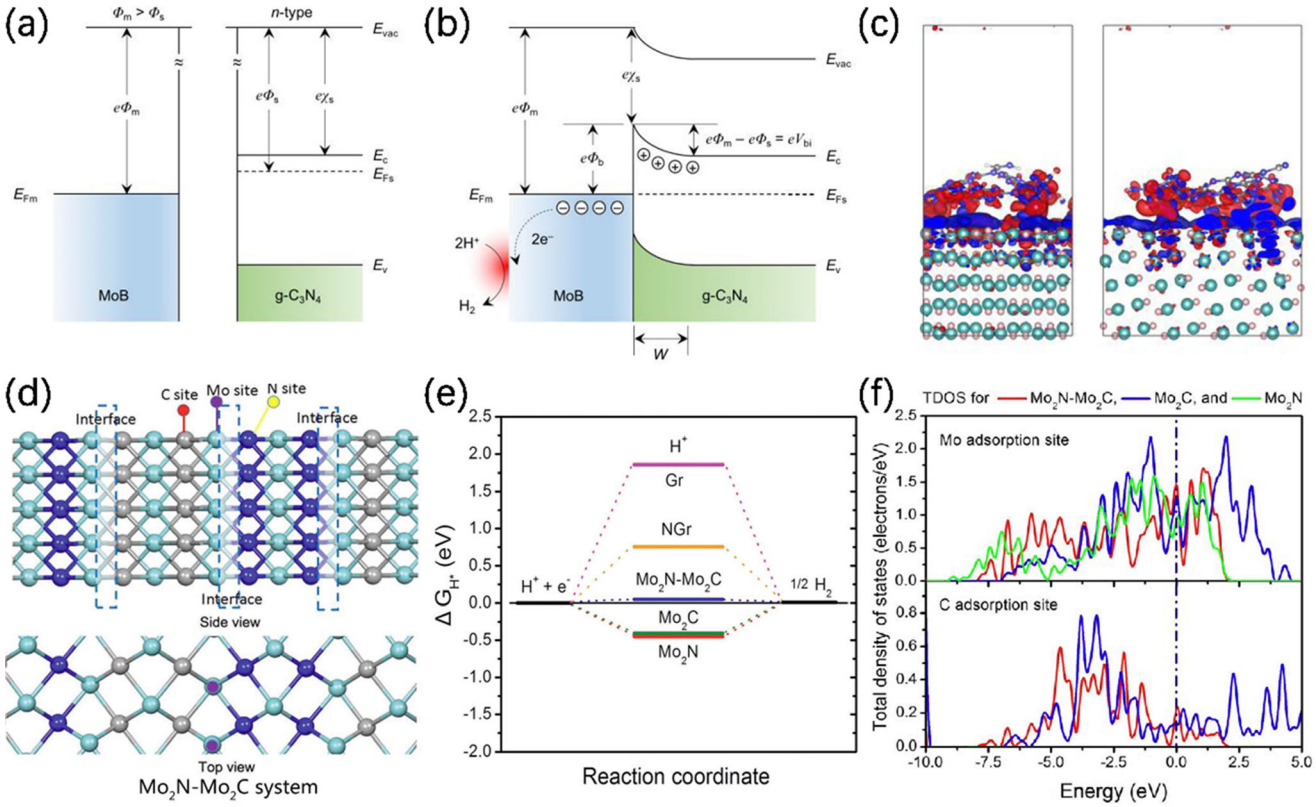

Figure 9. a) Band-structure diagrams of MoB and g-C_3N_4 (n-type semiconductor) before and b) after Mott–Schottky contact, where E_c denotes conduction band; E_{vac} denotes vacuum energy; E_F denotes Fermi level; E_v denotes valence band; χ denotes vacuum ionization energy; Φ denotes vacuum electrostatic potential;[162] Copyright 2018, Wiley-VCH. c) The charge density diagram of MoB/g-C_3N_4; d) The side view (top) and top view (bottom) of the Mo_2N-Mo_2C heterostructure; e) The HER energy profiles for the different active sites and f) the corresponding PDOS simulation results.[169] Copyright 2017, Wiley-VCH.

conductive materials as the substrates, since they exhibit superior electronic conductivity and are beneficial to the electron transporting between the electrode and reaction sites.[159,168,169] For example, instead of fabricating the stacked and aggregated heterostructures, Fu et al. synthesized a 2D in-plane WC/graphene heterostructure. This structure ensured the electrons transfer more efficiently between graphene and WC.[171–174] Consequently, the HER performance was improved with a remarkably lower Tafel slope of 38 mV dec^{-1}. In addition to the 2D structure, Ramakrishna et al. reported a 3D nanocomposite architecture of cobalt disulfide/reduced graphene oxide/carbon nanotubes (CoS_2/RGO/CNTs) as the HER catalyst,[32] where the 2D RGO and 1D CNTs could construct a 3D framework for electron transportation and the anchoring of CoS_2 nanoparticles. Consequently, this synergistic effect reduced the Tafel slope to 51 mV dec^{-1}. This result is better than most non-noble-metal electrocatalysts.

6. Conclusions and Outlook

In the last few decades, various functional inorganic namomaterials have been synthesized for energy conversion applications. The strategy of tuning the electronic states of nano-catalysts has become a vital way to accurately and controllably regulate the catalytic performance for electrocatalysts for water electrolysis and CO_2 reduction. In this Review, we summarized the working mechanisms of various atomic structures on the electronic structures and the corresponding catalytic capabilities of nanocatalysts.

In general, the intrinsic catalytic activity was determined by the adsorption ability of the active sites and the conductivity of the electrocatalysts. For the adsorption ability, a suitable adsorption energy can effectively reduce the overpotential of the catalytic process. The tailored electron density at the active sites, which could be caused by the polarization effect in the orbital coupling, results in an enhanced chemical adsorption ability. Some semi-empirical conclusions have been proposed, such as the SH principle and the d-band modulation theory. These semi-empirical conclusions emphasize the electron configuration and energy band structure for explaining the optimized adsorption ability. A better conductivity can efficiently transmit electrons from the electrode to the reactive interface and then accelerate sequential electrocatalytic processes. DOS investigations clearly illustrate the origin of the electron-conductive capacity from the perspective of band structure evolution, especially the band gap readjustment. It is well established that the electron obeys the Fermi–Dirac distribution. Thus,

© 2019 Wiley-VCH Verlag GmbH & Co. KGaA, Weinheim

These are not the final page numbers!

the narrowed or broken band gap can effectively boost the electron density in the conduction band, which directly contributes to enhancing the conductivity. In addition to the band gap readjustment, constructing a Schottky junction is another effective strategy to modulate the energy band structure for better charge transportation. The interfacial band bending caused by the Schottky contact effectively reduces the contact resistance and in turn facilitates the catalytic performance.

Despite the remarkable progresses in achieving high catalytic performance, several key challenges still remain. Firstly, the simulation-guided understanding of the reactivity mechanism still find it challenging to rationally demonstrate the adsorption ability and electronic behaviors. The results of DFT calculations show considerable dependence on the simulated conditions and methods during modeling and optimizing. In particular, there is no definite strategy to mimic the real electrolytic system with a liquid environment and a specific pH regime. Thus, a more complete theoretical system based on the actual electrochemical environment is needed. Secondly, another troublesome challenge is the problem of origin of the activity of the conversion to metal hydroxides/oxides on the surface of most OER catalyst, especially the sulfide, phosphide, and nitride catalysts. It cannot be simply defined as the real electrochemical property of the material itself. Nevertheless, in most cases, the structure reconstruction has not been incorporated and simulated theoretically when we illustrate the origin of activity. It is important that calculations track the complete process of catalytic reactions and show the evolution of activity through a rational model modification, which is then relevant for theory-guiding material synthesis. Thirdly, from the experimental perspective, further advanced in situ characterization methods are in great demand to unravel the active sites and the catalytic reaction process, which provide direct evidence for understanding the electronic behavior and electrocatalytic mechanism, as well as constructing theoretical models. With the operando-observed structural evolution information obtained during electrolytic processes, we can clearly build a bridge between catalytic activity and the electronic structure of the electrocatalyst, and set a direction for the development of novel non-noble-metal electrocatalysts with superior activity, selectivity and durability. For scaling-up the commercialization of electrocatalysis techniques, it is necessary to replace the noble-metal catalysts. In view of the importance of the basic theory and the application of electronic structure regulation in 2D materials, it is reasonable to extended these ideas to other challenging fields of energy conversion, catalysis and photoelectronic devices, including air-batteries, CO_2 and N_2 fixation, photoelectrochemical cells and photodetectors.

Acknowledgements

We gratefully acknowledge the support from the National Natural Science Foundation of China (51722204, 51802145), National Key Basic Research Program of China (2014CB931702), Sichuan Provincial Fund for Distinguished Young Academic and Technology Leaders (2014JQ0011), Sichuan Science and Technology Program (2016RZ0033, 2018RZ0082), and the Natural Science Foundation of Guangdong Province (2018A030310225).

Conflict of interest

The authors declare no conflict of interest.

[1] S. Chu, Y. Cui, N. Liu, *Nat. Mater.* **2017**, *16*, 16 – 22.
[2] M. S. Dresselhaus, I. L. Thomas, *Nature* **2001**, *414*, 332 – 337.
[3] M. K. Debe, *Nature* **2012**, *486*, 43 – 51.
[4] Z. W. Seh, J. Kibsgaard, C. F. Dickens, I. Chorkendorff, J. K. Nørskov, T. F. Jaramillo, *Science* **2017**, *355*, eaad4998.
[5] Y. Liu, C. Xiao, P. Huang, M. Cheng, Y. Xie, *Chem* **2018**, *4*, 1263 – 1283.
[6] J. Wang, W. Cui, Q. Liu, Z. Xing, A. M. Asiri, X. Sun, *Adv. Mater.* **2016**, *28*, 215 – 230.
[7] C. G. Morales-Guio, L. A. Stern, X. Hu, *Chem. Soc. Rev.* **2014**, *43*, 6555 – 6569.
[8] L. Han, S. Dong, E. Wang, *Adv. Mater.* **2016**, *28*, 9266 – 9291.
[9] B. Wu, N. Zheng, *Nano Today* **2013**, *8*, 168 – 197.
[10] D. Voiry, H. S. Shin, K. P. Loh, M. Chhowalla, *Nat. Rev. Chem.* **2018**, *2*, 0105.
[11] H. Zhang, G. Liu, L. Shi, J. Ye, *Adv. Energy Mater.* **2018**, *8*, 1701343.
[12] C. Zhu, S. Fu, Q. Shi, D. Du, Y. Lin, *Angew. Chem. Int. Ed.* **2017**, *56*, 13944 – 13960; *Angew. Chem.* **2017**, *129*, 14132 – 14148.
[13] J. Ahn, D. Wang, Y. Ding, J. Zhang, D. Qin, *ACS Nano* **2018**, *12*, 298 – 307.
[14] P. Strasser, M. Gliech, S. Kuehl, T. Moeller, *Chem. Soc. Rev.* **2018**, *47*, 715 – 735.
[15] X. Cui, C. Tang, Q. Zhang, *Adv. Energy Mater.* **2018**, *8*, 1800369.
[16] J. Zhang, J. Liu, L. Xi, Y. Yu, N. Chen, S. Sun, W. Wang, K. M. Lange, B. Zhang, *J. Am. Chem. Soc.* **2018**, *140*, 3876 – 3879.
[17] Y. Jiao, Y. Zheng, M. Jaroniec, S.-Z. Qiao, *Chem. Soc. Rev.* **2015**, *44*, 2060 – 2086.
[18] Y. Yan, B. Xia, B. Zhao, X. Wang, *J. Mater. Chem. A* **2016**, *4*, 17587 – 17603.
[19] G. Zhong, H. Wang, H. Yu, F. Peng, *Acta. Chim. Sin.* **2017**, *75*, 943 – 966.
[20] C. Guo, W. Liao, L. Sun, C. Chen, *Int. J. Electrochem. Sci.* **2015**, *10*, 2467 – 2477.
[21] M. E. G. Lyons, R. L. Doyle, D. Fernandez, I. J. Godwin, M. P. Browne, A. Rovetta, *Electrochem. Commun.* **2014**, *45*, 60 – 62.
[22] Y. Sun, S. Gao, F. Lei, Y. Xie, *Chem. Soc. Rev.* **2015**, *44*, 623 – 636.
[23] M. Blasco-Ahicart, J. Soriano-Lopez, J. J. Carbo, J. M. Poblet, J. R. Galan-Mascaros, *Nat. Chem.* **2018**, *10*, 24 – 30.
[24] J. Hwang, R. Rao, L. Giordano, Y. Katayama, Y. Yu, Y. Shao-Horn, *Science* **2017**, *358*, 751 – 756.
[25] S. Kaya, D. Friebel, H. Ogasawara, T. Anniyev, A. Nilsson, *J. Electron Spectrosc. Relat. Phenom.* **2013**, *190*, 113 – 124.
[26] D. Yan, Y. Li, J. Huo, R. Chen, L. Dai, S. Wang, *Adv. Mater.* **2017**, *29*, 1606459.
[27] J. Xie, H. Zhang, S. Li, R. Wang, X. Sun, M. Zhou, J. Zhou, X. Lou, Y. Xie, *Adv. Mater.* **2013**, *25*, 5807 – 5813.
[28] L. Zhang, Y. Jia, G. Gao, X. Yan, N. Chen, J. Chen, M. Soo, B. Wood, D. Yang, A. Du, X. Yao, *Chem* **2018**, *4*, 285 – 297.
[29] Y. Zhu, Z. Chen, W. Zhou, S. Jiang, J. Zou, Z. Shao, *ChemSusChem* **2013**, *6*, 2249 – 2254.

 © 2019 Wiley-VCH Verlag GmbH & Co. KGaA, Weinheim

[30] Y. Yin, J. Han, Y. Zhang, X. Zhang, P. Xu, Q. Yuan, L. Samad, X. Wang, Y. Wang, Z. Zhang, P. Zhang, X. Cao, B. Song, S. Jin, *J. Am. Chem. Soc.* **2016**, *138*, 7965 – 7972.

[31] Y. Wang, T. Zhou, K. Jiang, P. Da, Z. Peng, J. Tang, B. Kong, W.-B. Cai, Z. Yang, G. Zheng, *Adv. Energy Mater.* **2014**, *4*, 1400696.

[32] S. Peng, L. Li, X. Han, W. Sun, M. Srinivasan, S. G. Mhaisalkar, F. Cheng, Q. Yan, J. Chen, S. Ramakrishna, *Angew. Chem. Int. Ed.* **2014**, *53*, 12594 – 12599; *Angew. Chem.* **2014**, *126*, 12802 – 12807.

[33] A. Lucas, K. C. Fong, *J. Phys. Condens. Matter* **2018**, *30*, 053001.

[34] L. Zhang, Q. Xu, J. Niu, Z. Xia, *Phys. Chem. Chem. Phys.* **2015**, *17*, 16733 – 16743.

[35] I. Jeon, S. Zhang, L. Zhang, H. J. Choi, J. M. Seo, Z. Xia, L. Dai, J. B. Baek, *Adv. Mater.* **2013**, *25*, 6138 – 6145.

[36] Y. Jiang, L. Yang, T. Sun, J. Zhao, Z. Lyu, O. Zhuo, X. Wang, Q. Wu, J. Ma, Z. Hu, *ACS Catal.* **2015**, *5*, 6707 – 6712.

[37] T. Reier, M. Oezaslan, P. Strasser, *ACS Catal.* **2012**, *2*, 1765 – 1772.

[38] S. Cherevko, S. Geiger, O. Kasian, N. Kulyk, J. P. Grote, A. Savan, B. R. Shrestha, S. Merzlikin, B. Breitbach, A. Ludwig, K. J. J. Mayrhofer, *Catal. Today* **2016**, *262*, 170 – 180.

[39] H. Tao, L. Fang, J. Chen, H. Yang, J. Gao, J. Miao, S. Chen, B. Liu, *J. Am. Chem. Soc.* **2016**, *138*, 9978 – 9985.

[40] F. Calle-Vallejo, N. G. Inoglu, H. Y. Su, J. I. Martinez, I. C. Man, M. T. M. Koper, J. R. Kitchin, J. Rossmeisl, *Chem. Sci.* **2013**, *4*, 1245 – 1249.

[41] J. O. M. Bockris, T. Otagawa, *J. Electrochem. Soc.* **1984**, *131*, 290 – 302.

[42] J. Suntivich, H. A. Gasteiger, N. Yabuuchi, H. Nakanishi, J. B. Goodenough, Y. Shao-Horn, *Nat. Chem.* **2011**, *3*, 546 – 550.

[43] J. Suntivich, K. J. May, H. A. Gasteiger, J. B. Goodenough, Y. Shao-Horn, *Science* **2011**, *334*, 1383 – 1385.

[44] V. Tripkovic, H. A. Hansen, J. M. Garcia-Lastra, T. Vegge, *J. Phys. Chem. C* **2018**, *122*, 1135 – 1147.

[45] C. Chen, G. King, R. M. Dickerson, P. A. Papin, S. Gupta, W. R. Kellogg, G. Wu, *Nano Energy* **2015**, *13*, 423 – 432.

[46] D. N. Mueller, M. L. Machala, H. Bluhm, W. C. Chueh, *Nat. Commun.* **2015**, *6*, 6097.

[47] Y. Zhu, W. Zhou, J. Yu, Y. Chen, M. Liu, Z. Shao, *Chem. Mater.* **2016**, *28*, 1691 – 1697.

[48] Y. Guo, Y. Tong, P. Chen, K. Xu, J. Zhao, Y. Lin, W. Chu, Z. Peng, C. Wu, Y. Xie, *Adv. Mater.* **2015**, *27*, 5989 – 5994.

[49] J. Kim, X. Yin, K. C. Tsao, S. Fang, H. Yang, *J. Am. Chem. Soc.* **2014**, *136*, 14646 – 14649.

[50] X. Yu, X. Lou, *Adv. Energy Mater.* **2018**, *8*, 1701592.

[51] L. Xu, Q. Jiang, Z. Xiao, X. Li, J. Huo, S. Wang, L. Dai, *Angew. Chem. Int. Ed.* **2016**, *55*, 5277 – 5281; *Angew. Chem.* **2016**, *128*, 5363 – 5367.

[52] F. Y. Cheng, T. R. Zhang, Y. Zhang, J. Du, X. P. Han, J. Chen, *Angew. Chem. Int. Ed.* **2013**, *52*, 2474 – 2477; *Angew. Chem.* **2013**, *125*, 2534 – 2537.

[53] Z. Xu, J. R. Kitchin, *Catal. Commun.* **2014**, *52*, 60 – 64.

[54] J. Huang, H. Gao, Y. Xia, Y. Sun, J. Xiong, Y. Li, S. Cong, J. Guo, S. Du, G. Zou, *Nano Energy* **2018**, *46*, 305 – 313.

[55] Q. Lu, Y. Yu, Q. Ma, B. Chen, H. Zhang, *Adv. Mater.* **2016**, *28*, 1917 – 1933.

[56] J. Zhang, S. Liu, H. Liang, R. Dong, X. Feng, *Adv. Mater.* **2015**, *27*, 7426 – 7431.

[57] G. W. Shim, W. Hong, S. Yang, S. Y. Choi, *J. Mater. Chem. A* **2017**, *5*, 14950 – 14968.

[58] Y. Liu, H. Cheng, M. Lyu, S. Fan, Q. Liu, W. Zhang, Y. Zhi, C. Wang, C. Xiao, S. Wei, B. Ye, Y. Xie, *J. Am. Chem. Soc.* **2014**, *136*, 15670 – 15675.

[59] F. Wang, T. A. Shifa, X. Zhan, Y. Huang, K. Liu, Z. Cheng, C. Jiang, J. He, *Nanoscale* **2015**, *7*, 19764 – 19788.

[60] H. Li, C. Tsai, A. L. Koh, L. Cai, A. W. Contryman, A. H. Fragapane, J. Zhao, H. S. Han, H. C. Manoharan, F. Abild-Pedersen, J. K. Nørskov, X. Zheng, *Nat. Mater.* **2016**, *15*, 48 – 53.

[61] J. Huang, Y. Sun, Y. Zhang, G. Zou, C. Yan, S. Cong, T. Lei, X. Dai, J. Guo, R. Lu, Y. Li, J. Xiong, *Adv. Mater.* **2018**, *30*, 1705045.

[62] Y. Zhao, R. Nakamura, K. Kamiya, S. Nakanishi, K. Hashimoto, *Nat. Commun.* **2013**, *4*, 2390.

[63] T. Ma, J. Ran, S. Dai, M. Jaroniec, S. Qiao, *Angew. Chem. Int. Ed.* **2015**, *54*, 4646 – 4650; *Angew. Chem.* **2015**, *127*, 4729 – 4733.

[64] J. Xie, J. Zhang, S. Li, F. Grote, X. Zhang, H. Zhang, R. Wang, Y. Lei, B. Pan, Y. Xie, *J. Am. Chem. Soc.* **2013**, *135*, 17881 – 17888.

[65] T. Kou, T. Smart, B. Yao, I. Chen, D. Thota, Y. Ping, Y. Li, *Adv. Energy Mater.* **2018**, *8*, 1703538.

[66] F. Calle-Vallejo, J. I. Martinez, J. Rossmeisl, *Phys. Chem. Chem. Phys.* **2011**, *13*, 15639 – 15643.

[67] G. Fazio, L. Ferrighi, D. Perilli, C. Di Valentin, *Int. J. Quantum Chem.* **2016**, *116*, 1623 – 1640.

[68] J. Deng, H. Li, J. Xiao, Y. Tu, D. Deng, H. Yang, H. Tian, J. Li, P. J. Ren, X. Bao, *Energy Environ. Sci.* **2015**, *8*, 1594 – 1601.

[69] X. Sun, J. Dai, Y. Guo, C. Wu, F. Hu, J. Zhao, X. Zeng, Y. Xie, *Nanoscale* **2014**, *6*, 8359 – 8367.

[70] X. Liu, W. Xi, C. Li, X. Li, J. Shi, Y. Shen, J. He, L. Zhang, L. Xie, X. Sun, P. Wang, J. Luo, L.-M. Liu, Y. Ding, *Nano Energy* **2018**, *44*, 371 – 377.

[71] D. He, G. He, H. Jiang, Z. Chen, M. Huang, *Chem. Commun.* **2017**, *53*, 5132 – 5135.

[72] C. Ling, L. Shi, Y. Ouyang, X. Zeng, J. Wang, *Nano Lett.* **2017**, *17*, 5133 – 5139.

[73] J. Zhuo, M. Caban-Acevedo, H. Liang, L. Samad, Q. Ding, Y. Fu, M. Li, S. Jin, *ACS Catal.* **2015**, *5*, 6355 – 6361.

[74] G. Wu, P. Zelenay, *Acc. Chem. Res.* **2013**, *46*, 1878 – 1889.

[75] H. Zhang, S. Hwang, M. Wang, Z. Feng, S. Karakalos, L. Luo, Z. Qiao, X. Xie, C. Wang, D. Su, Y. Shao, G. Wu, *J. Am. Chem. Soc.* **2017**, *139*, 14143 – 14149.

[76] G. Wu, K. L. More, C. M. Johnston, P. Zelenay, *Science* **2011**, *332*, 443 – 447.

[77] G. Wu, A. Santandreu, W. Kellogg, S. Gupta, O. Ogoke, H. Zhang, H. Wang, L. Dai, *Nano Energy* **2016**, *29*, 83 – 110.

[78] H. Fei, J. Dong, Y. Feng, C. S. Allen, C. Wan, B. Volosskiy, M. Li, Z. Zhao, Y. Wang, H. Sun, P. An, W. Chen, Z. Guo, C. Lee, D. Chen, I. Shakir, M. Liu, T. Hu, Y. Li, A. I. Kirkland, X. Duan, Y. Huang, *Nat. Catal.* **2018**, *1*, 63 – 72.

[79] L. L. Fan, P. F. Liu, X. C. Yan, L. Gu, Z. Z. Yang, H. G. Yang, S. L. Qiu, X. D. Yao, *Nat. Commun.* **2016**, *7*, 10667.

[80] K. Liu, H. Zhong, F. Meng, X. Zhang, J. Yan, Q. Jiang, *Mater. Chem. Front.* **2017**, *1*, 2155 – 2173.

[81] Y. Jiao, Y. Zheng, M. Jaroniec, S.-Z. Qiao, *J. Am. Chem. Soc.* **2014**, *136*, 4394 – 4403.

[82] P. Strasser, S. Koh, T. Anniyev, J. Greeley, K. More, C. Yu, Z. Liu, S. Kaya, D. Nordlund, H. Ogasawara, M. F. Toney, A. Nilsson, *Nat. Chem.* **2010**, *2*, 454 – 460.

[83] D. Voiry, H. Yamaguchi, J. Li, R. Silva, D. C. Alves, T. Fujita, M. Chen, T. Asefa, V. B. Shenoy, G. Eda, M. Chhowalla, *Nat. Mater.* **2013**, *12*, 850 – 855.

[84] W. Tang, G. Henkelman, *J. Chem. Phys.* **2009**, *130*, 194504.

[85] M. Mavrikakis, B. Hammer, J. K. Nørskov, *Phys. Rev. Lett.* **1998**, *81*, 2819 – 2822.

[86] J. Wang, M. Yan, K. Zhao, X. Liao, P. Wang, X. Pan, W. Yang, L. Mai, *Adv. Mater.* **2017**, *29*, 1604464.

[87] H. Wang, S. Xu, C. Tsai, Y. Li, C. Liu, J. Zhao, Y. Liu, H. Yuan, F. Abild-Pedersen, F. B. Prinz, J. K. Nørskov, Y. Cui, *Science* **2016**, *354*, 1031 – 1036.

[88] G. Gao, Y. Jiao, F. Ma, Y. Jiao, E. Waclawik, A. Du, *J. Catal.* **2015**, *332*, 149 – 155.

© 2019 Wiley-VCH Verlag GmbH & Co. KGaA, Weinheim

These are not the final page numbers!

[89] M. Li, Z. Zhao, T. Cheng, A. Fortunelli, C.-Y. Chen, R. Yu, Q. Zhang, L. Gu, B. V. Merinov, Z. Lin, E. Zhu, T. Yu, Q. Jia, J. Guo, L. Zhang, W. A. Goddard III, Y. Huang, X. Duan, *Science* **2016**, *354*, 1414 – 1419.

[90] T. Ling, D. Yan, H. Wang, Y. Jiao, Z. Hu, Y. Zheng, L. Zheng, J. Mao, H. Liu, X. Du, M. Jaroniec, S.-Z. Qiao, *Nat. Commun.* **2017**, *8*, 1509.

[91] J. Wu, L. Qi, H. You, A. Gross, J. Li, H. Yang, *J. Am. Chem. Soc.* **2012**, *134*, 11880 – 11883.

[92] H. Li, M. Du, M. J. Mleczko, A. L. Koh, Y. Nishi, E. Pop, A. J. Bard, X. Zheng, *J. Am. Chem. Soc.* **2016**, *138*, 5123 – 5129.

[93] S. Kwon, K. Shin, K. Bang, H. Y. Kim, H. M. Lee, *Phys. Chem. Chem. Phys.* **2016**, *18*, 13232 – 13238.

[94] Q. Feng, S. Zhao, D. He, S. Tian, L. Gu, X. Wen, C. Chen, Q. Peng, D. Wang, Y. Li, *J. Am. Chem. Soc.* **2018**, *140*, 2773 – 2776.

[95] G. Gao, G. Sun, A. Du, *J. Phys. Chem. C* **2016**, *120*, 16761 – 16766.

[96] A. Fortunelli, W. A. Goddard III, L. Sementa, G. Barcaro, F. R. Negreiros, A. Jaramillo-Botero, *Chem. Sci.* **2015**, *6*, 3915 – 3925.

[97] B. Hammer, J. K. Nørskov, *Nature* **1995**, *376*, 238 – 240.

[98] B. Hammer, J. K. Nørskov, *Adv. Catal.* **2000**, *45*, 71 – 129.

[99] B. Hammer, J. K. Nørskov, *Surf. Sci.* **1995**, *343*, 211 – 220.

[100] S. Schnur, A. Gross, *Phys. Rev. B* **2010**, *81*, 033402.

[101] M. F. Francis, W. A. Curtin, *Nat. Commun.* **2015**, *6*, 6261.

[102] D. Wang, H. Xin, R. Hovden, H. Wang, Y. Yu, D. A. Muller, F. J. DiSalvo, H. D. Abruna, *Nat. Mater.* **2013**, *12*, 81 – 87.

[103] S. Zhang, X. Zhang, G. Jiang, H. Zhu, S. Guo, D. Su, G. Lu, S. Sun, *J. Am. Chem. Soc.* **2014**, *136*, 7734 – 7739.

[104] M. W. Small, S. I. Sanchez, N. S. Marinkovic, A. I. Frenkel, R. G. Nuzzo, *ACS Nano* **2012**, *6*, 5583 – 5595.

[105] Z. Zhang, Z. Luo, B. Chen, C. Wei, J. Zhao, J. Chen, X. Zhang, Z. Lai, Z. Fan, C. Tan, M. Zhao, Q. Lu, B. Li, Y. Zong, C. Yan, G. Wang, Z. Xu, H. Zhang, *Adv. Mater.* **2016**, *28*, 8712 – 8717.

[106] X. Wang, L. Figueroa-Cosme, X. Yang, M. Luo, J. Liu, Z. Xie, Y. Xia, *Nano Lett.* **2016**, *16*, 1467 – 1471.

[107] T. Ghosh, M. B. Vukmirovic, F. J. DiSalvo, R. R. Adzic, *J. Am. Chem. Soc.* **2010**, *132*, 906 – 907.

[108] F. Liu, C. Wu, G. Yang, S. Yang, *J. Phys. Chem. C* **2015**, *119*, 15500 – 15505.

[109] L. Bu, N. Zhang, S. Guo, X. Zhang, J. Li, J. Yao, T. Wu, G. Lu, J. Ma, D. Su, X. Huang, *Science* **2016**, *354*, 1410 – 1414.

[110] K. Liang, Y. Yan, L. Guo, K. Marcus, Z. Li, L. Zhou, Y. Li, R. Ye, N. Orlovskaya, Y.-H. Sohn, Y. Yang, *ACS Energy Lett.* **2017**, *2*, 1315 – 1320.

[111] D. B. Putungan, S.-H. Lin, J.-L. Kuo, *Phys. Chem. Chem. Phys.* **2015**, *17*, 21702 – 21708.

[112] X. Chen, G. Wang, *Phys. Chem. Chem. Phys.* **2016**, *18*, 9388 – 9395.

[113] Z. Sui, X. Li, Z. Sun, H. Tao, P. Zhang, L. Zhao, B. Han, *Carbon* **2018**, *126*, 111 – 118.

[114] S. Yang, X. Feng, X. Wang, K. Mullen, *Angew. Chem. Int. Ed.* **2011**, *50*, 5339 – 5343; *Angew. Chem.* **2011**, *123*, 5451 – 5455.

[115] L. Wei, H. E. Karahan, K. Goh, W. Jiang, D. Yu, O. Birer, R. Jiang, Y. Chen, *J. Mater. Chem. A* **2015**, *3*, 7210 – 7214.

[116] G. Wu, Y. Hu, Y. Liu, J. Zhao, X. Chen, V. Whoehling, C. Plesse, G. T. Nguyen, F. Vidal, W. Chen, *Nat. Commun.* **2015**, *6*, 7258.

[117] M. Du, L. Cui, Y. Cao, A. J. Bard, *J. Am. Chem. Soc.* **2015**, *137*, 7397 – 7403.

[118] R. Yang, J. Leisch, P. Strasser, M. F. Toney, *Chem. Mater.* **2010**, *22*, 4712 – 4720.

[119] J. Greeley, I. E. Stephens, A. S. Bondarenko, T. P. Johansson, H. A. Hansen, T. F. Jaramillo, J. Rossmeisl, I. Chorkendorff, J. K. Nørskov, *Nat. Chem.* **2009**, *1*, 552 – 556.

[120] V. Stamenkovic, B. S. Mun, K. J. Mayrhofer, P. N. Ross, N. M. Markovic, J. Rossmeisl, J. Greeley, J. K. Nørskov, *Angew. Chem. Int. Ed.* **2006**, *45*, 2897 – 2901; *Angew. Chem.* **2006**, *118*, 2963 – 2967.

[121] P. Hernandez-Fernandez, F. Masini, D. N. McCarthy, C. E. Strebel, D. Friebel, D. Deiana, P. Malacrida, A. Nierhoff, A. Bodin, A. M. Wise, J. H. Nielsen, T. W. Hansen, A. Nilsson, I. E. Stephens, I. Chorkendorff, *Nat. Chem.* **2014**, *6*, 732 – 738.

[122] M. Escudero-Escribano, P. Malacrida, M. H. Hansen, U. G. Vej-Hansen, A. Velazquez-Palenzuela, V. Tripkovic, J. Schiotz, J. Rossmeisl, I. E. Stephens, I. Chorkendorff, *Science* **2016**, *352*, 73 – 76.

[123] W. Sun, Z. Zhou, W. Q. Zaman, L. Cao, J. Yang, *ACS Appl. Mater. Interfaces* **2017**, *9*, 41855 – 41862.

[124] K. Amakawa, L. Sun, C. Guo, M. Havecker, P. Kube, I. E. Wachs, S. Lwin, A. I. Frenkel, A. Patlolla, K. Hermann, R. Schlögl, A. Trunschke, *Angew. Chem. Int. Ed.* **2013**, *52*, 13553 – 13557; *Angew. Chem.* **2013**, *125*, 13796 – 13800.

[125] Y. Tan, P. Liu, L. Chen, W. Cong, Y. Ito, J. Han, X. Guo, Z. Tang, T. Fujita, A. Hirata, M. Chen, *Adv. Mater.* **2014**, *26*, 8023 – 8028.

[126] A. Castellanos-Gomez, R. Roldan, E. Cappelluti, M. Buscema, F. Guinea, H. S. van der Zant, G. A. Steele, *Nano Lett.* **2013**, *13*, 5361 – 5366.

[127] E. Scalise, M. Houssa, G. Pourtois, V. Afanas'ev, A. Stesmans, *Nano Res.* **2012**, *5*, 43 – 48.

[128] H. Pan, Y. Zhang, *J. Phys. Chem. C* **2012**, *116*, 11752 – 11757.

[129] C. Xu, S. Peng, C. Tan, H. Ang, H. Tan, H. Zhang, Q. Yan, *J. Mater. Chem. A* **2014**, *2*, 5597 – 5601.

[130] L. Kou, C. Tang, Y. Zhang, T. Heine, C. Chen, T. Frauenheim, *J. Phys. Chem. Lett.* **2012**, *3*, 2934 – 2941.

[131] K. Yan, S. K. Kim, A. Khorshidi, P. R. Guduru, A. A. Peterson, *J. Phys. Chem. C* **2017**, *121*, 6177 – 6183.

[132] M. Yan, X. Pan, P. Wang, F. Chen, L. He, G. Jiang, J. Wang, J. Liu, X. Xu, X. Liao, J. Yang, L. Mai, *Nano Lett.* **2017**, *17*, 4109 – 4115.

[133] R. S. Berry, B. M. Smirnov, *Phys.-Usp.* **2009**, *52*, 137 – 164.

[134] Y. Chai, G. An, Y. Liu, C. Liu, *Prog. Chem.* **2007**, *19*, 234 – 242.

[135] P. Chen, K. Xu, S. Tao, T. Zhou, Y. Tong, H. Ding, L. Zhang, W. Chu, C. Wu, Y. Xie, *Adv. Mater.* **2016**, *28*, 7527 – 7532.

[136] Q. Tang, D. Jiang, *ACS Catal.* **2016**, *6*, 4953 – 4961.

[137] H. Wang, Z. Lu, S. Xu, D. Kong, J. Cha, G. Zheng, P. C. Hsu, K. Yan, D. Bradshaw, F. B. Prinz, Y. Cui, *Proc. Natl. Acad. Sci. USA* **2013**, *110*, 19701 – 19706.

[138] D. Voiry, M. Salehi, R. Silva, T. Fujita, M. Chen, T. Asefa, V. B. Shenoy, G. Eda, M. Chhowalla, *Nano Lett.* **2013**, *13*, 6222 – 6227.

[139] J. A. Woollam, R. B. Somoano, *Phys. Rev. B* **1976**, *13*, 3843 – 3853.

[140] L. Wang, Z. Xu, W. Wang, X. Bai, *J. Am. Chem. Soc.* **2014**, *136*, 6693 – 6697.

[141] A. N. Enyashin, G. Seifert, *Comput. Theor. Chem.* **2012**, *999*, 13 – 20.

[142] M. Kan, J. Wang, X. Li, S. Zhang, Y. Li, Y. Kawazoe, Q. Sun, P. Jena, *J. Phys. Chem. C* **2014**, *118*, 1515 – 1522.

[143] G. Gao, Y. Jiao, F. Ma, Y. Jiao, E. Waclawik, A. Du, *J. Phys. Chem. C* **2015**, *119*, 13124 – 13128.

[144] K. A. Duerloo, Y. Li, E. J. Reed, *Nat. Commun.* **2014**, *5*, 4214.

[145] Y. Lin, D. O. Dumcenco, Y. Huang, K. Suenaga, *Nat. Nanotechnol.* **2014**, *9*, 391 – 396.

[146] Y. Kang, S. Najmaei, Z. Liu, Y. Bao, Y. Wang, X. Zhu, N. J. Halas, P. Nordlander, P. M. Ajayan, J. Lou, Z. Fang, *Adv. Mater.* **2014**, *26*, 6467 – 6471.

[147] Y. Gong, J. Lin, X. Wang, G. Shi, S. Lei, Z. Lin, X. Zou, G. Ye, R. Vajtai, B. I. Yakobson, H. Terrones, M. Terrones, B. K. Tay, J. Lou, S. T. Pantelides, Z. Liu, W. Zhou, P. M. Ajayan, *Nat. Mater.* **2014**, *13*, 1135 – 1142.

[148] C. Huang, S. Wu, A. M. Sanchez, J. J. Peters, R. Beanland, J. S. Ross, P. Rivera, W. Yao, D. H. Cobden, X. Xu, *Nat. Mater.* **2014**, *13*, 1096 – 1101.

© 2019 Wiley-VCH Verlag GmbH & Co. KGaA, Weinheim

[149] X. Duan, C. Wang, J. C. Shaw, R. Cheng, Y. Chen, H. Li, X. Wu, Y. Tang, Q. Zhang, A. Pan, J. Jiang, R. Yu, Y. Huang, X. Duan, *Nat. Nanotechnol.* **2014**, *9*, 1024 – 1030.
[150] F. Wypych, R. Schollhorn, *J. Chem. Soc. Chem. Commun.* **1992**, 1386 – 1388.
[151] A. N. Enyashin, L. Yadgarov, L. Houben, I. Popov, M. Weidenbach, R. Tenne, M. Bar-Sadan, G. Seifert, *J. Phys. Chem. C* **2011**, *115*, 24586 – 24591.
[152] Z. Xu, J. R. Kitchin, *Phys. Chem. Chem. Phys.* **2015**, *17*, 28943 – 28949.
[153] C. Tsai, K. R. Chan, J. K. Nørskov, F. Abild-Pedersen, *Surf. Sci.* **2015**, *640*, 133 – 140.
[154] J. Bonde, P. G. Moses, T. F. Jaramillo, J. K. Nørskov, I. Chorkendorff, *Faraday Discuss.* **2009**, *140*, 219 – 231.
[155] X.-L. Fan, Y. Yang, P. Xiao, W.-M. Lau, *J. Mater. Chem. A* **2014**, *2*, 20545 – 20551.
[156] P. Liu, J. A. Rodriguez, *J. Am. Chem. Soc.* **2005**, *127*, 14871 – 14878.
[157] G.-F. Chen, T. Ma, Z.-Q. Liu, N. Li, Y.-Z. Su, K. Davey, S.-Z. Qiao, *Adv. Funct. Mater.* **2016**, *26*, 3314 – 3323.
[158] Z. Jin, P. Li, D. Xiao, *Green Chem.* **2016**, *18*, 1459 – 1464.
[159] Y. Jia, L. Zhang, G. Gao, H. Chen, B. Wang, J. Zhou, M. T. Soo, M. Hong, X. Yan, G. Qian, J. Zou, A. Du, X. Yao, *Adv. Mater.* **2017**, *29*, 1700017.
[160] A. Wu, Y. Xie, H. Ma, C. Tian, Y. Gu, H. Yan, X. Zhang, G. Yang, H. Fu, *Nano Energy* **2018**, *44*, 353 – 363.
[161] J. Huang, Y. Sun, X. Du, Y. Zhang, C. Wu, C. Yan, Y. Yan, G. Zou, W. Wu, R. Lu, Y. Li, J. Xiong, *Adv. Mater.* **2018**, *30*, 1803367.
[162] J. Hou, Y. Sun, Y. Wu, S. Cao, L. Sun, *Adv. Funct. Mater.* **2018**, *28*, 1704447.
[163] M. R. Nellist, F. A. Laskowski, F. Lin, T. J. Mills, S. W. Boettcher, *Acc. Chem. Res.* **2016**, *49*, 733 – 740.
[164] Z. Zhuang, Y. Li, Z. Li, F. Lv, Z. Lang, K. Zhao, L. Zhou, L. Moskaleva, S. Guo, L. Mai, *Angew. Chem. Int. Ed.* **2018**, *57*, 496 – 500; *Angew. Chem.* **2018**, *130*, 505 – 509.
[165] J. Huang, Y. Su, Y. Zhang, W. Wu, C. Wu, Y. Sun, R. Lu, G. Zou, Y. Li, J. Xiong, *J. Mater. Chem. A* **2018**, *6*, 9467 – 9472.
[166] H. Li, K. Yu, C. Li, Z. Tang, B. Guo, X. Lei, H. Fu, Z. Zhu, *Sci. Rep.* **2015**, *5*, 18730.
[167] S. Tang, W. Wu, S. Zhang, D. Ye, P. Zhong, X. Li, L. Liu, Y. Li, *Phys. Chem. Chem. Phys.* **2018**, *20*, 1861 – 1871.
[168] J. P. Shi, X. B. Zhou, G. F. Han, M. X. Liu, D. L. Ma, J. Y. Sun, C. Li, Q. Q. Ji, Y. Zhang, X. J. Song, X. Y. Lang, Q. Jiang, Z. F. Liu, Y. F. Zhang, *Adv. Mater. Interfaces* **2016**, *3*, 1600332.
[169] H. Yan, Y. Xie, Y. Jiao, A. Wu, C. Tian, X. Zhang, L. Wang, H. Fu, *Adv. Mater.* **2018**, *30*, 1704156.
[170] V. Anisimov, Y. Izyumov in *Springer Series in Solid-State Sciences*, vol. 163 (Eds.: M. Cardona, P. Fulde, K. von Klitzing, R. Merlin, H.-J. Queisser, H. Stormer), Springer, Berlin, Heidelberg, **2010**, pp. 47 – 120.
[171] M. Zeng, Y. Chen, J. Li, H. Xue, R. Mendes, J. Liu, T. Zhang, M. H. Ruemmeli, L. Fu, *Nano Energy* **2017**, *33*, 356 – 362.
[172] Y. Ge, H. Bai, C. Li, P. Guan, L. Wu, D. Xu, Y. Hong, W. Fan, W. Shi, *New J. Chem.* **2017**, *41*, 3460 – 3465.
[173] T. Grewe, X. Deng, H. Tuysuz, *Chem. Mater.* **2014**, *26*, 3162 – 3168.
[174] J. Huang, Y. Li, Y. Xia, J. Zhu, Q. Yi, H. Wang, J. Xiong, Y. Sun, G. Zou, *Nano Res.* **2017**, *10*, 1010 – 1020.

Manuscript received: September 3, 2018
Revised manuscript received: September 28, 2018
Accepted manuscript online: October 1, 2018
Version of record online: ■■ ■■, ■■■■

 © 2019 Wiley-VCH Verlag GmbH & Co. KGaA, Weinheim

These are not the final page numbers!

Reviews

Water Splitting

X. Du, J. Huang,* J. Zhang, Y. Yan, C. Wu, Y. Hu, C. Yan, T. Lei, W. Chen, C. Fan,* J. Xiong* ——— ■■■–■■■

Modulating Electronic Structures of Inorganic Nanomaterials for Efficient Electrocatalytic Water Splitting

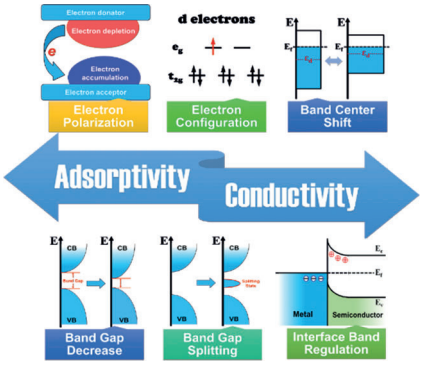

Making split happen: Strategies to regulate electronic structures of materials to optimize their electrocatalytic activities in water splitting are summarized in this Review. The structure–electronic-behavior–activity relationships are highlighted as well as current challenges on understanding the electronic behaviors.

© 2019 Wiley-VCH Verlag GmbH & Co. KGaA, Weinheim

View publication stats